



# Application of PDF Modeling to Swirling and Nonswirling Turbulent Jets

P.R. VAN SLOOTEN

*United Technologies Research Center, 411 Silver Lane, MS 129-16,  
East Hartford, CT 06108, U.S.A.*

S.B. POPE

*Sibley School of Mechanical and Aerospace Engineering, Cornell University,  
Ithaca, NY 14853, U.S.A.*

Received 7 May 1998; accepted in revised form 23 June 1999

**Abstract.** The turbulence modeling in probability density function (PDF) methods is studied through applications to turbulent swirling and nonswirling co-axial jets and to the temporal shear layer. The PDF models are formulated at the level of either the joint PDF of velocity and turbulent frequency or the joint PDF of velocity, wave vector, and turbulent frequency. The methodology of wave vector models (WVMs) is based on an exact representation of rapidly distorted homogeneous turbulence, and several models are constructed in a previous paper [1]. A revision to a previously presented conditional-mean turbulent frequency model [2] is constructed to improve the numerical implementation of the model for inhomogeneous turbulent flows. A pressure transport model is also implemented in conjunction with several velocity models. The complete model yields good comparisons with available experimental data for a low swirl case. The individual models are also assessed in terms of their significance to an accurate solution of the co-axial jets, and a comparison is made to a similar assessment for the temporal shear layer. The crucial factor in determining the quality of the co-axial jet simulations is demonstrated to be the proper specification of a parameter ratio in the modeled source of turbulent frequency. The parameter specification is also shown to be significant in the temporal shear layer.

**Key words:** PDF modeling, turbulence modeling, swirling flows.

## 1. Introduction

The modeling of turbulence is required for all computationally tractable methods of simulating complex turbulent flows. In probability density function (PDF) methods, the turbulence modeling achieves closure at the level of one-point, one-time joint PDFs. The approach proves advantageous for turbulent reacting flows, because the crucial processes of convection and reaction are treated without modeling assumption [3, 4]. In contrast, standard moment closure methods such as  $k$ - $\varepsilon$  models and Reynolds stress models (RSMs) do not supply sufficient information to treat finite-rate, nonlinear reactions and must apply a gradient transport hypothesis to model some convective processes.

The exact equations for the joint PDFs, as derived from the Navier–Stokes equation, contain unclosed terms that require modeling. For example, in the equation for the joint PDF of velocity and composition, the effects of the fluctuating pressure gradient, the dissipation of the velocity fluctuations by molecular viscosity, and the mixing of species by molecular diffusion are not closed. Closure is achieved in the standard implementation of PDF methods through stochastic models for the behavior of fluid particles which are simulated numerically through Monte Carlo techniques [3, 4].

The modeled PDFs contain a vast amount of statistical information, but the turbulence modeling is most usefully examined at the level of the Reynolds stress equation. The unclosed terms in the velocity–composition joint PDF equation correspond to the rapid and slow pressure–rate-of-strain correlations, the pressure transport, and the dissipation tensor in the Reynolds stress equations. The pressure–rate-of-strain correlation is modeled through a stochastic equation for the fluid particle’s velocity. The simplified Langevin model (SLM) by Pope [5] and various forms of the generalized Langevin model (GLM) by Haworth and Pope [6]; Pope [7]; and Wouters et al. [8] are velocity models that can be directly related to RSMs. These models are applied to numerous inhomogeneous flows in [2, 9–18].

Reynolds stress models have difficulty in reliably predicting inhomogeneous turbulent flows with rotation [19–21], which is typically traced to the modeling of the rapid pressure–rate-of-strain correlation. The wave vector model (WVM) class of PDF methods for inhomogeneous turbulent flows has been developed by Van Slooten and Pope [1] and Van Slooten et al. [2] to address this issue. The WVM represents without modeling assumption homogeneous turbulence in the limit of rapid distortions (RDT) and is based on the particle representation model for RDT of Kassinos and Reynolds [22]. Since the only “unclosed” term in the RDT limit at the level of Reynolds stress closures is the rapid pressure–rate-of-strain correlation, the model provides an exact expression for this correlation in the RDT limit. Additional modeling is necessary for non-RDT homogeneous turbulent flows and for inhomogeneous turbulent flows, and several models are constructed in [1].

In RSMs, the pressure transport is typically considered negligible, while the turbulent convective transport is modeled through a gradient transport hypothesis. However, the direct numerical simulation (DNS) data of Rogers and Moser [23] for a temporal shear layer illustrate that the pressure transport and turbulent convective transport of the Reynolds stresses nearly balance across the layer and are the dominant terms at the edge of the layer. The combined pressure and turbulent convective transport is thereby of minor significance, and RSMs perform quite well in this respect. In PDF methods, the turbulent convective transport is treated exactly, and neglecting the pressure transport yields an imbalance that alters the growth of the layer. In [2], a PDF model is developed for the pressure transport in general free shear flows that is based on Lumley’s [24] model for the pressure-velocity city correlation.

Time or length scale information on a turbulent flow is required to close turbulence models. For example, the modeled mean dissipation is often used in moment closure methods. A particle turbulent frequency model for PDF methods is an alternative approach that provides more information for modeling the complex behavior of internal and external (turbulent-nonturbulent) intermittency. In [25, 26] a stochastic dissipation model is developed that specifies the turbulent time scale as the inverse of the particle turbulent frequency. The model produces a lognormal PDF of dissipation and directly addresses the issue of internal intermittency, but it requires *ad hoc* models for the important physical phenomena of entrainment and external intermittency. In [2, 27], an alternative method is developed that specifies the inverse of the turbulent time scale through a conditional-mean of the turbulent frequency. The conditional-mean represents the mean of only the turbulent particles which provides a natural treatment of external intermittency. The conditional-mean method also yields simple stochastic equations that are subject to smaller statistical fluctuations than the lognormal dissipation model in the Monte Carlo simulation. Particle turbulent frequency models have been applied to various inhomogeneous flows in [2, 10, 14, 15, 17, 18, 28].

A revised form of the particle turbulent frequency model is introduced here primarily to facilitate the numerical implementation of the conditional-mean model. In the previous model, the production of turbulent frequency is modeled in terms of the mean rate of strain squared, which results in poor numerical convergence [29]. Specifically, the term leads to bias\* that increases as the spatial grid is refined, and therefore a large number of computational particles is required to reduce the bias to acceptable levels. In the revised model, the production of turbulent frequency is directly related to the production of turbulent kinetic energy – a formulation that circumvents the problem of bias. An investigation is also performed on a new definition of the conditional-mean that takes into account the inhomogeneous production and transport of the normalized variance of turbulence frequency. In the flows considered, the effects of the new definition are not found to be significant, and it is presented only to illustrate the robust nature of the conditional mean model.

The purpose of this paper is to continue the development and validation of the WVM and the conditional-mean turbulent frequency model for inhomogeneous turbulent flows. The primary cases studied are the swirling and nonswirling co-axial jets from the experiments by Takahashi and co-workers [30, 31]. Previous velocity/turbulent-frequency PDF calculations of these flows are reported by Anand et al. [10] who used the SLM, the stochastic dissipation model, and the boundary layer approximation. In these calculations, the model parameters were altered from the standard values specified by Pope [26] for free shear flows. In the current work, the WVM and the revised form of the conditional-mean turbulent frequency model are used, and the full recirculating-flow PDF equations are solved.

---

\* Bias is a deterministic error that arises in the Monte Carlo implementation of stochastic equations with a finite number of particles,  $N$ . It decreases as  $1/N$ .

The new form of the turbulent frequency model is also demonstrated in a temporal shear layer through comparisons with the DNS data for a temporal shear layer [23] and the experimental data of a plane mixing layer [32]. Identical model parameters are used in both the temporal shear layer and the co-axial jets to demonstrate the increased robustness of the current models.

The turbulence modeling performed in this work is discussed in Section 2 which contains: a brief introduction to PDF methods in Section 2.1; a summary of the particle velocity models including a description of the pressure transport model in Section 2.2; and the revised form of the conditional-mean turbulent frequency model in Section 2.3. The discussion of the numerical results for both the temporal shear layer and swirling and nonswirling co-axial jets is contained in Section 3, and finally the conclusions are presented in Section 4.

## 2. Turbulence Modeling

### 2.1. PDF FORMULATION

Only an overview of PDF methods for incompressible, inhomogeneous turbulent flows is provided here as detailed presentations of PDF methods are available in [3, 4]. The PDFs of interest in this work are the joint PDF of velocity and turbulent frequency and the joint PDF of velocity, wave vector, and turbulent frequency. In the standard approach to PDF modeling and simulation, a model for the evolution equation of the joint PDF is developed whose solution is obtained via a particle/Monte Carlo simulation. This method requires the derivation of a set of stochastic equations that represent the behavior of the particles.

For inhomogeneous flows, a model for the particle position,  $\mathbf{X}^*(t)$ , is required,

$$\frac{dX_i^*}{dt} = U_i^*(t), \quad (1)$$

where the particle velocity,  $\mathbf{U}^*(t)$ , evolves by an additional stochastic differential equation. The particle velocity models are discussed in Section 2.2. One particle velocity model, the wave vector model (WVM), also requires an additional particle property, the wave vector  $\mathbf{e}^*(t)$ , which adds a state-space wave vector to the independent variables in the joint PDF. The turbulent frequency  $\omega^*(t)$  also evolves by a stochastic differential equation, and effects the particle velocity model through the specification of the turbulent time scale. Section 2.3 contains a detailed presentation of the particle turbulent frequency model.

The stochastic system of equations is solved using PDF2DV [33] which implements a Monte Carlo technique via a particle/mesh method. The mesh is used to estimate the local Eulerian mean values (e.g.,  $\langle \mathbf{U} \rangle$ ,  $k$ , and  $\tau$ ) which are required as coefficients in the stochastic equations. The velocity statistics are calculated by a cloud-in-cell kernel estimation with bilinear basis functions [34], while a velocity/pressure correction algorithm [35] is implemented to impose the consist-

ency condition, mean mass conservation, and the Poisson equation for the mean pressure.

## 2.2. VELOCITY MODELS

The particle velocity models implemented in this work are the simplified Langevin model (SLM), the Lagrangian isotropization of production model (LIPM), and the WVM. These models are presented here with further details provided in the references.

The SLM is a basic particle velocity model that is commonly implemented. The particle velocity evolves by the stochastic differential equation

$$dU_i^* = -\frac{\partial \langle P \rangle}{\partial x_i} dt - \left[ \frac{1}{2} + \frac{3}{4} C_0 \right] [U_i^* - \langle U_i \rangle] \frac{dt}{\tau} + \sqrt{\frac{C_0 k}{\tau}} dW_i, \quad (2)$$

where  $C_0 = 2.1$  is a model parameter,  $\mathbf{W}(t)$  is an isotropic, vector-valued Wiener process, and the Eulerian mean modified pressure  $\langle P \rangle$ , the Eulerian mean velocity  $\langle U_i \rangle$ , the turbulent time scale  $\tau$ , and the turbulent kinetic energy  $k$  are evaluated at  $(\mathbf{x}, t) = (\mathbf{X}^*[t], t)$ . At the Reynolds stress level, the SLM models the return-to-isotropy tensor via Rotta's model and neglects the rapid pressure–rate-of-strain tensor.

In many turbulent flows, the rapid pressure–rate-of-strain is a dominant term, and numerous models have been developed at the Reynolds stress level of closure [6, 36–42]. A Lagrangian version of the first Launder, Reece, and Rodi model, which is a combination of the isotropization of production model (IP model) of Naot et al. [36] and Rotta's model, is implemented here. From the generalized Langevin model [6], the LIPM developed in [7] is

$$dU_i^* = -\frac{\partial \langle P \rangle}{\partial x_i} dt + G_{ij} [U_j^* - \langle U_j \rangle] dt + \sqrt{\frac{C_0 k}{\tau}} dW_i, \quad (3)$$

where

$$G_{ij} \equiv \frac{1}{\tau} [\alpha_1 \delta_{ij} + \alpha_2 (b_{ij} - 3b_{ij}^2)] + C_2 S_{ij} + W_{ij} - 3(1 - C_2) b_{ik} W_{jk} \quad (4)$$

and\*

$$\alpha_1 = -\left( \frac{1}{2} + \frac{3}{4} C_0 \right) + 3\alpha_2 b_{ll}^3 + \frac{1}{2} C_2 \frac{P}{\varepsilon}. \quad (5)$$

The mean velocity gradients enter this model through the mean rate of strain tensor  $S_{ij} \equiv [\partial \langle U_i \rangle / \partial x_j + \partial \langle U_j \rangle / \partial x_i] / 2$ , the mean rate of rotation tensor  $W_{ij} \equiv [\partial \langle U_i \rangle / \partial x_j - \partial \langle U_j \rangle / \partial x_i] / 2$ , and the production of turbulent kinetic energy  $P \equiv -\langle u_i u_j \rangle \partial \langle U_i \rangle / \partial x_j$ . The model parameters are defined by  $\alpha_2 = 3.5$  and

\*  $b_{ij}^2$  is defined as  $b_{ik} b_{kj}$ , and  $b_{ll}^3$  as  $b_{lk} b_{kj} b_{jl}$ .

$C_2 = 0.6$ . The LIPM exactly represents the IP model for the rapid pressure–rate-of-strain correlation, but differs slightly from the standard version of Rotta’s model by implementing a functional form for its model coefficient.

The wave vector models from Van Slooten and Pope [1] provide an exact representation of rapidly distorted homogeneous turbulence and are based on the particle representation model for RDT by Kassinos and Reynolds [22]. The model for RDT is extended to homogeneous turbulence away from the RDT limit and to inhomogeneous turbulence through models for the dissipation and the return-to-isotropy tensor and through the addition of a particle position and mean velocity [1]. A particular WVM, the Langevin velocity model, is selected for this work and is expressed as

$$\begin{aligned} dU_i^* = & -\frac{\partial \langle P \rangle}{\partial x_i} dt + 2 \frac{\partial \langle U_m \rangle}{\partial x_n} [e_i^* e_m^* u_n^* - \langle e_i^* e_m^* u_n^* \rangle] dt - \left[ \frac{1}{2} + \frac{3}{4} a_u \right] u_i^* \frac{dt}{\tau} \\ & + \gamma [b_{ij} - b_{ll}^2 \delta_{ij}] u_j^* \frac{dt}{\tau} + \sqrt{\frac{a_u k}{\tau}} dW_i \end{aligned} \quad (6)$$

and

$$\begin{aligned} de_i^* = & -\frac{\partial \langle U_m \rangle}{\partial x_n} e_m^* [\delta_{in} - e_i^* e_n^*] dt - \frac{1}{2} \left[ a_e + a_u \frac{k}{u_s^* u_s^*} \right] e_i^* \frac{dt}{\tau} \\ & - \gamma [\delta_{ij} - e_i^* e_j^*] b_{jl} e_l^* \frac{dt}{\tau} - \sqrt{\frac{a_u k}{\tau}} \frac{u_i^* e_l^*}{u_s^* u_s^*} dW_l \\ & + \sqrt{\frac{a_e}{\tau}} \left[ \delta_{il} - e_i^* e_l^* - \frac{u_i^* u_l^*}{u_s^* u_s^*} \right] dW'_l + Q_i, \end{aligned} \quad (7)$$

where  $\mathbf{W}(t)$  and  $\mathbf{W}'(t)$  are independent, vector-valued Wiener processes, and  $a_u = 2.1$ ,  $a_e = 0.03$ , and  $\gamma = 2.0$  are model parameters. The vector  $\mathbf{Q}$  is uniquely defined as the projection that maintains the orthogonality between the particle wave vector and the particle velocity. It represents the effects of the flow’s inhomogeneity on the wave vector.

In PDF methods the turbulent convective transport is treated without modeling assumption, while the pressure transport has been traditionally neglected. However, the DNS data of Rogers and Moser [23] demonstrate that the pressure and turbulent convective transport nearly balance each other across a temporal shear layer and are the dominant terms at the edge of the layer. In [2] a model for the pressure transport is developed based on Lumley’s model [24] for the velocity–pressure correlation. The model is implemented through an additional term in the particle velocity equation,

$$dU_i^* = C_{pt} \left[ \frac{u_s^* u_s^*}{2k} - 1 \right] \frac{\partial k}{\partial x_i} dt + \dots, \quad (8)$$

where  $C_{pt} = 0.12$  for the WVM and  $C_{pt} = 0.2$  for the LIPM. The results from Van Slooten et al. [2] demonstrate the vital importance of such a model in the case of a

temporal shear layer. It should be noted that this model for pressure transport does not behave exactly like a transport term (i.e., the divergence of a flux), but is better estimated as a sink of kinetic energy.

### 2.3. TURBULENT FREQUENCY MODEL

Modeled evolution equations for the turbulent kinetic energy, the Reynolds stress tensor, and the velocity PDF require turbulent scale information for closure. One approach is to model a turbulent time scale information in the PDF formulation through a particle turbulent frequency  $\omega^*$ . The joint PDF of velocity and turbulent frequency contains more statistical information than modeled mean equations (i.e., the standard dissipation model), and this information is then available for more sophisticated modeling of complex turbulent flows.

Two types of velocity/turbulent-frequency models from previous works are differentiated by their interaction with the particle velocity equation. Pope and co-workers [25, 26] construct turbulent frequency models for homogeneous and inhomogeneous turbulence, respectively, where the time scale of a particle is defined as the inverse of the particle turbulent frequency. The motivation of the approach is to represent internal intermittency through a model that yields a lognormal distribution for a modeled instantaneous dissipation. The entrainment of nonturbulent fluid and external intermittency are treated via *ad hoc* models [26]. These models are tested in free shear flows [15, 26] and in swirling flows [10]. Despite providing fairly good results, the turbulent frequency and refined Langevin models are complicated and computationally expensive. The long tails of the lognormal distribution hamper the convergence of the Monte Carlo solution of the modeled PDF equations, because of the large statistical fluctuations that they cause. In addition, the *ad hoc* models represent phenomena that are typically of greater importance to turbulence modeling than internal intermittency.

#### 2.3.1. Basic construction of frequency model

The model applied here is based on the work of Jayesh and Pope [27] which is also presented in [2]. In this method, a conditional-mean turbulent frequency,  $\Omega$ , represents the inverse of the turbulence time scale in the particle velocity model,  $\Omega = \tau^{-1} \equiv \varepsilon/k$ . The conditional-mean models the mean of the *turbulent* particles and differs from the mean of all particles  $\langle \omega \rangle$  in a turbulent-nonturbulent region. The result is a simple and efficient model that treats turbulent entrainment and external intermittency in a natural manner. The model is applied to various free shear flows in [2, 16–18, 28]. A refinement of the approach is developed here to provide a better representation of inhomogeneous turbulent flows and to improve the numerical implementation of particle turbulent frequency models.

The stochastic model of Van Slooten et al. [2] for the turbulent frequency  $\omega^*$  is

$$d\omega^* = -C_3[\omega^* - \langle \omega \rangle]\Omega dt - \omega^* S_\omega \langle \omega \rangle dt + \sqrt{2C_3 C_4 \omega^* \langle \omega \rangle \Omega} dW'', \quad (9)$$

where  $C_3$  and  $C_4$  are constant model parameters,  $S_\omega$  is the source of turbulent frequency, and  $W''(t)$  is an independent Wiener process. In statistically-stationary, homogeneous turbulence (i.e., where  $S_\omega = 0$ ), the model provides a gamma distribution for the PDF of turbulent frequency with mean  $\langle \omega^* \rangle = \langle \omega \rangle$  and with variance  $\text{var}(\omega^*) = C_4 \langle \omega \rangle^2$ . The DNS data of Yeung and Pope [43] suggest that  $C_4$  is Reynolds number dependent with  $C_4 \sim 1$  for a range of Taylor-scale Reynolds numbers,  $\text{Re}_\lambda \sim 38\text{--}93$ . The parameter is here set to a constant value  $C_4 = 0.25$  to improve the numerical implementation of the model by forcing a gamma distribution with relatively small variance and short tails. The other parameter is also set to a constant value  $C_3 = 1.0$  [2].

The mean turbulent frequency  $\langle \omega \rangle$  multiplying the source of turbulent frequency  $S_\omega$ , in the particle equation, Equation (9), acts as a time scale to the model. In the other modeled terms of the particle equation, the conditional-mean turbulent frequency is used as the time scale. To provide consistency the first modification of the original model of Jayesh and Pope [27] is to set the conditional-mean as the time scale throughout the model,

$$d\omega^* = -C_3[\omega^* - \langle \omega \rangle]\Omega dt - \omega^* S_\omega \Omega dt + \sqrt{2C_3 C_4 \omega^* \langle \omega \rangle \Omega} dW''. \quad (10)$$

The effects of this modification are minor for all flows tested and are not discussed further in this work.

### 2.3.2. Definition of conditional frequency $\Omega$

The conditional-mean turbulent frequency  $\Omega$  is constructed to model the mean turbulent frequency of just the turbulent fluid and is defined to be proportional to the above-average mean [27]

$$\Omega \equiv C_\Omega \langle \omega^* \mid \omega^* \geq \langle \omega \rangle \rangle. \quad (11)$$

The coefficient  $C_\Omega$  is chosen with the goal of forcing  $\Omega = \langle \omega \rangle$  in fully turbulent regions, while allowing  $\Omega > \langle \omega \rangle$  in turbulent-nonturbulent intermittent regions. If  $\omega^*$  has a gamma distribution with a normalized variance  $\sigma^2 \equiv \text{var}(\omega^*)/\langle \omega \rangle^2$ , then the requirement  $\Omega = \langle \omega \rangle$  determines the coefficient  $C_\Omega$  to be

$$C_\Omega = q \frac{\Gamma(q, q)}{\Gamma(q + 1, q)}, \quad (12)$$

where  $q \equiv 1/\sigma^2$  and  $\Gamma(q, q)$  is the incomplete gamma function. The coefficient is shown as a function of the normalized variance in Figure 1. In previous work, it was set to the value of  $C_\Omega = 0.6893$  corresponding to the stationary homogeneous value of the normalized variance,  $\sigma^2 = C_4 = 0.25$ .

In homogeneous turbulence, the normalized variance of turbulent frequency evolves by

$$\frac{d\sigma^2}{dt} = -2\Omega C_3(\sigma^2 - C_4), \quad (13)$$

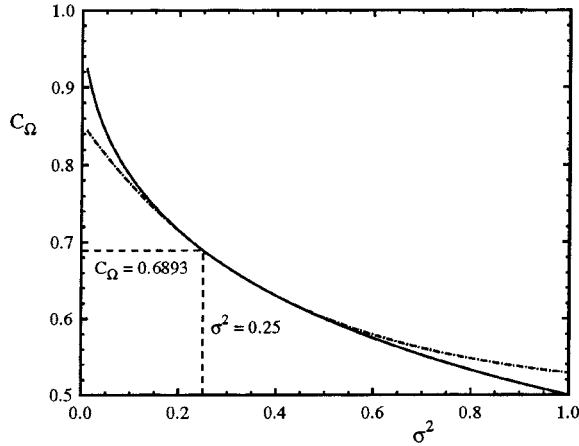


Figure 1. The coefficient  $C_\Omega$  as a function of the normalized variance  $\sigma^2$ : —, defined by Equation (12); and ---, modeled by Equation (15).

so that  $\sigma^2$  relaxes to the specified value  $C_4$ . For inhomogeneous turbulence the modeled evolution equation contains additional transport and production terms that alter the stationary solution,

$$\frac{\partial \sigma^2}{\partial t} + \langle U_k \rangle \frac{\partial \sigma^2}{\partial x_k} = - \underbrace{\frac{1}{\langle \omega \rangle^2} \frac{\partial \langle u_k \omega'^2 \rangle}{\partial x_k}}_{\text{turbulent transport}} + \underbrace{\frac{2\sigma^2}{\langle \omega \rangle} \frac{\partial \langle u_k \omega' \rangle}{\partial x_k}}_{\text{transport}} - \underbrace{\frac{2\langle u_k \omega' \rangle}{\langle \omega \rangle^2} \frac{\partial \langle \omega \rangle}{\partial x_k}}_{\text{production}} - \underbrace{2\Omega C_3 (\sigma^2 - C_4)}_{\text{source}}, \quad (14)$$

where  $\omega'$  is the fluctuating turbulent frequency. Consequently, for inhomogeneous flows, the variance  $\sigma^2$  does not in general relax to  $C_4$ , and is often found to be much larger.

Calculations of a temporal shear layer (described below) are used to illustrate this point. Figure 2 shows the profile of the normalized variance as a function of  $\xi$ , where  $\xi \equiv y/\delta_m$  is the cross-stream position,  $y$ , normalized by the momentum thickness,  $\delta_m$ . The normalized variance  $\sigma^2$  is larger than 0.25 across the entire layer and is very large at the edge of the layer where a bimodal distribution exists between the turbulent and nonturbulent particles. Figure 3 shows that the turbulent frequency maintains a gamma distribution even towards the edge of the layer up to  $\xi \approx 2$  where  $\sigma^2 \approx 0.7$ . The  $y = x$  line in Figure 3 corresponds to a gamma distribution with the local value of the normalized variance. The variations from this line are not significant until the tail of the distribution,  $\omega^* \sim 4\langle \omega \rangle$ , where the measured statistics are poor.

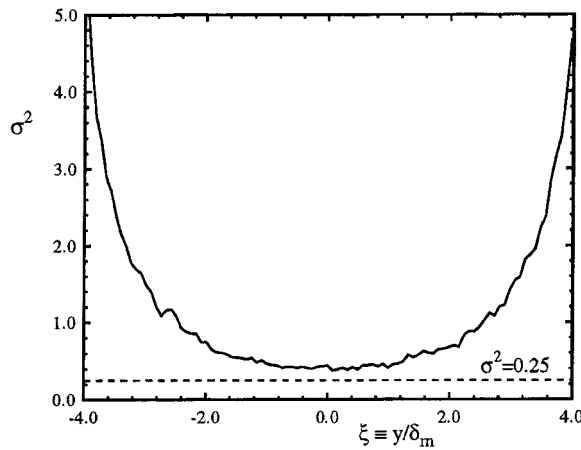


Figure 2. Profile of the normalized variance of turbulence frequency across the temporal shear layer from TSa in Table IV.

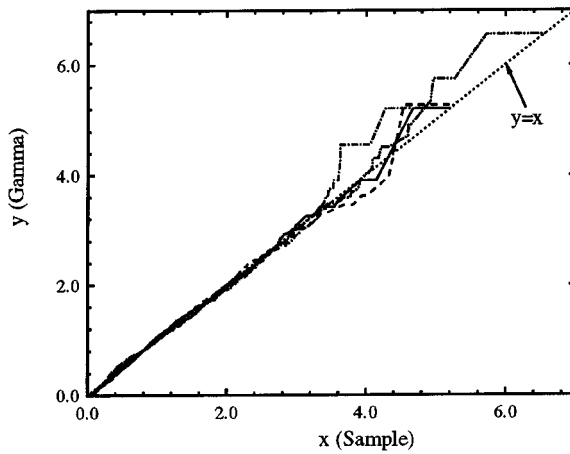


Figure 3.  $Q-Q$  plot for the distributions of normalized particle turbulent frequency from TSa in Table IV. Given  $x, y$  is defined implicitly by  $\text{Prob}[\phi < x] = \text{Prob}[G < y]$ , where  $\phi \equiv \omega^*/\langle\omega\rangle$  is the normalized turbulent frequency and  $G$  is a gamma random variable with the same variance as  $\phi$ . The distributions are for particles in the following ranges of cross-stream position: —,  $\xi = (0.00, 0.07)$ ; ---,  $\xi = (1.31, 1.37)$ ; -·-,  $\xi = (1.89, 1.96)$ .

An alternative specification of the coefficient  $C_\Omega$  is devised to account for the inhomogeneous distribution of the normalized variance within the fully turbulent region, while maintaining a representation for the turbulent mean in turbulent-nonturbulent intermittent region. A variable form is constructed to match Equation (12) over a range of a  $\sigma^2$  with an asymptote to a nonzero constant

$$C_\Omega = 0.5 + 0.3537 \exp(-2.5\sigma^2). \quad (15)$$

As may be seen from Figure 1, the model in Equation (15) asymptotes to 0.5 and provides good agreement with Equation (12) over the range  $\sigma^2 \in (0.1, 0.6)$  which corresponds to the central part of the temporal shear layer ( $|\xi| \leq 1.8$  in Figure 2).

In summary, a variable form of  $C_\Omega$  is required to maintain  $\Omega = \langle \omega \rangle$  within fully turbulent regions of inhomogeneous flows due to the variations in  $\sigma^2$ . Equation (12) is derived from  $\Omega = \langle \omega \rangle$  and an assumed gamma distribution of particle turbulent frequency. However, the conditional mean turbulent frequency is designed to model the mean of the turbulent particles in turbulent-nonturbulent intermittent regions (i.e.,  $\Omega > \langle \omega \rangle$ ), where Equation (12) is not appropriate. Equation (15) is constructed to model Equation (12) over a limited range in values of  $\sigma^2$ , and to asymptote with increasing  $\sigma^2$  to a nonzero constant, 0.5.

### 2.3.3. Mean source of turbulent frequency

The source of the turbulent frequency is defined from the standard dissipation model [44] for homogeneous turbulence

$$S_\omega = C_{\omega 2} - C_{\omega 1} \frac{P}{\varepsilon} = C_{\omega 2} - C_{\omega 1} \frac{P}{k\Omega}, \quad (16)$$

where  $C_{\omega 1} \equiv C_{\varepsilon 1} - 1$  and  $C_{\omega 2} \equiv C_{\varepsilon 2} - 1$  are model constants. The  $k$ - $\varepsilon$  model form of the production was used in the previous references as an alternate model for the source

$$S_\omega = C_{\omega 2} - C_1 \frac{S_{ij} S_{ij}}{\langle \omega \rangle^2}, \quad (17)$$

where  $C_1$  is a model parameter. The production-to-dissipation model parameter  $C_{\omega 1}$  is related to  $C_1$  through the definition of the coefficient  $C_\mu$  in the gradient transport assumption,  $C_1 = 2C_\mu C_{\omega 1}$ . The standard value for the coefficient,  $C_\mu = 0.09$ , is used to compare the parameters from the different models in the work that follows.

In the modeled turbulent kinetic energy equation from PDF methods, the production is treated explicitly. The model based on the true production-to-dissipation ratio, Equation (16), provides a stronger relationship between the production of turbulent kinetic energy and turbulent frequency than one that uses the  $k$ - $\varepsilon$  surrogate, Equation (17). The square of the strain rate  $S_{ij} S_{ij}$  has also been demonstrated to be a strong source of grid dependency in the bias [29]. The variance of the statistical fluctuations in the production-to-dissipation ratio is smaller than in the square of the strain rate, which decreases the bias. Numerical studies of the model are currently being implemented.

The turbulent kinetic energy is sensitive to the values selected for the parameters in the modeled source of turbulent frequency. In homogeneous turbulence, production and dissipation completely control the evolution of the turbulent kinetic

Table I. Suggested model parameters for the original and revised conditional-mean turbulent frequency models.

$\omega^*$ Model <sup>1</sup>	$\mathbf{u}^*$ Model	$C_{\omega 1}^2$	$C_{\omega 2}$	$C_{\omega 2}/C_{\omega 1}$
$S_{\omega} - P$	WVM	0.5625	0.9	1.6
$S_{\omega} - P$	LIPM	0.5625	0.9	1.6
$S_{\omega} - S$	WVM	0.3333	0.9	2.7
$S_{\omega} - S$	LIPM	0.4444	0.9	2.0

<sup>1</sup>The notation  $S_{\omega} - P$  refers to the Model Of Equation (16), while  $S_{\omega} - S$  refers to that of Equation (17).

<sup>2</sup>Assumes  $C_{\mu} = 0.09$  in the original model.

energy, and their ratio in the revised model has a well-known stationary state that is fully determined by the model parameters

$$\left(\frac{P}{\varepsilon}\right)_{\infty} = \frac{C_{\omega 2}}{C_{\omega 1}}. \quad (18)$$

For inhomogeneous turbulence, the transport terms alter the stationary state of the production-to-dissipation ratio and affect the ratio's impact on the kinetic energy. However, the ratio of  $C_{\omega 2}$  to  $C_{\omega 1}$  remains an important parameter.

The standard values of the parameters were specified by Launder et al. [37] for RSMs, where the turbulent transport of turbulent frequency is modeled via a gradient transport hypothesis. The parameter  $C_{\omega 1}$  was optimized to 0.44 (i.e.,  $C_{\omega 1} = 1.44$ ) through numerical experimentation using a RSM, while the parameter  $C_{\omega 2}$  was set to 0.9 (i.e.,  $C_{\omega 2} = 1.9$ ) through analytical comparisons with experimental data in decaying grid turbulence. The resulting production-to-dissipation ratio in homogeneous turbulence,  $(P/\varepsilon)_{\infty} \approx 2.0$ , is higher than experimental and DNS data for homogeneous flows where values of  $(P/\varepsilon)_{\infty} \approx 1.4$ – $1.8$  are more typical. In PDF methods, all convective terms including the turbulent transport of turbulent frequency are treated explicitly, and the standard specification of  $C_{\omega 1}$  is no longer optimal. Suggested parameter values that produce reasonable results for the temporal shear layer and co-axial jets considered, are provided in Table I for both the original and revised conditional mean-turbulent frequency models. The value  $C_{\omega 2} = 0.9$  is used throughout, and the effects of the ratio  $C_{\omega 2}/C_{\omega 1}$  are examined in Section 3 by altering the value of  $C_{\omega 1}$ .

In summary, the turbulent frequency model employed here consists of the stochastic differential equation, Equation (10), with the conditional mean turbulent frequency  $\Omega$  defined by Equation (11). The performance of the model is studied for different specifications of the coefficient  $C_{\Omega}$  and for different forms of the source term  $S_{\omega}$ . The specifications of the coefficient  $C_{\Omega}$  are  $C_{\Omega}$ -fixed (i.e.,  $C_{\Omega} = 0.6893$ ) and  $C_{\Omega}$ -variable (i.e., Equation (15)), while the forms of the source term  $S_{\omega}$ , are  $S_{\omega} - S$  (i.e., Equation (17)) and  $S_{\omega} - P$  (i.e., Equation (16)).

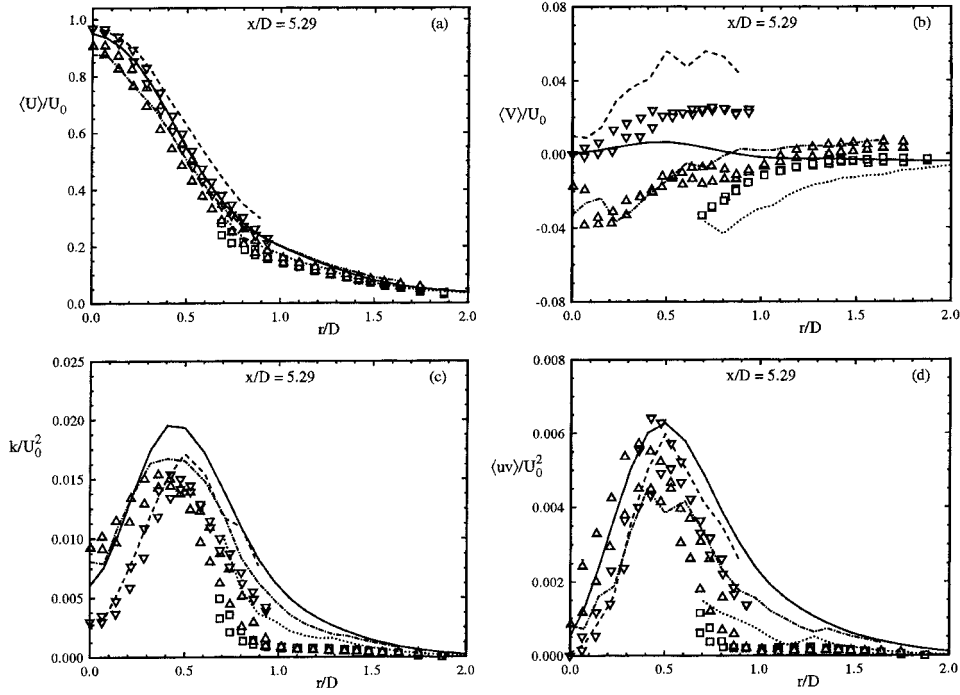


Figure 4. Representative profiles for conditional statistics in the nonswirling co-axial jet at  $x/D = 5.29$  from case L0a (lines) and experimental data (symbols) of Takahashi and Vangness [30] with: —, unconditional statistics; and statistics conditional on: (---,  $\nabla$ ), jet flow; (---,  $\Delta$ ), annular flow; and (- · - ·,  $\square$ ), co-flow.

### 3. Results and Discussions

#### 3.1. CONFINED SWIRLING AND NONSWIRLING CO-AXIAL TURBULENT JETS

Simulations are performed on the co-axial jets studied experimentally by Takahashi and co-workers [30, 31]. The flow consists of a central air jet of diameter  $D = 9.45$  mm, an annular air jet of diameter  $D_a = 26.92$  mm, and an external co-flow of air in a square duct of side  $s = 150$  mm with rounded corners. Swirl is imparted to the annular jet by a helical vane swirler of varying angles which is located 96 mm upstream of the inlet. The swirl number is a measure of the strength of the swirl and is defined as the ratio of the axial flux of angular momentum to the product of the axial flux of axial momentum and the radius,

$$S \equiv \frac{2 \int_0^{D_a/2} \rho \langle U \rangle \langle W \rangle r^2 dr}{D_a \int_0^{D_a/2} \rho \langle U \rangle^2 r dr}, \quad (19)$$

where  $\langle U \rangle$  and  $\langle W \rangle$  are the Eulerian mean axial and tangential velocities. The experimental cases are summarized in Table II with the swirl number calculated near the inlet.

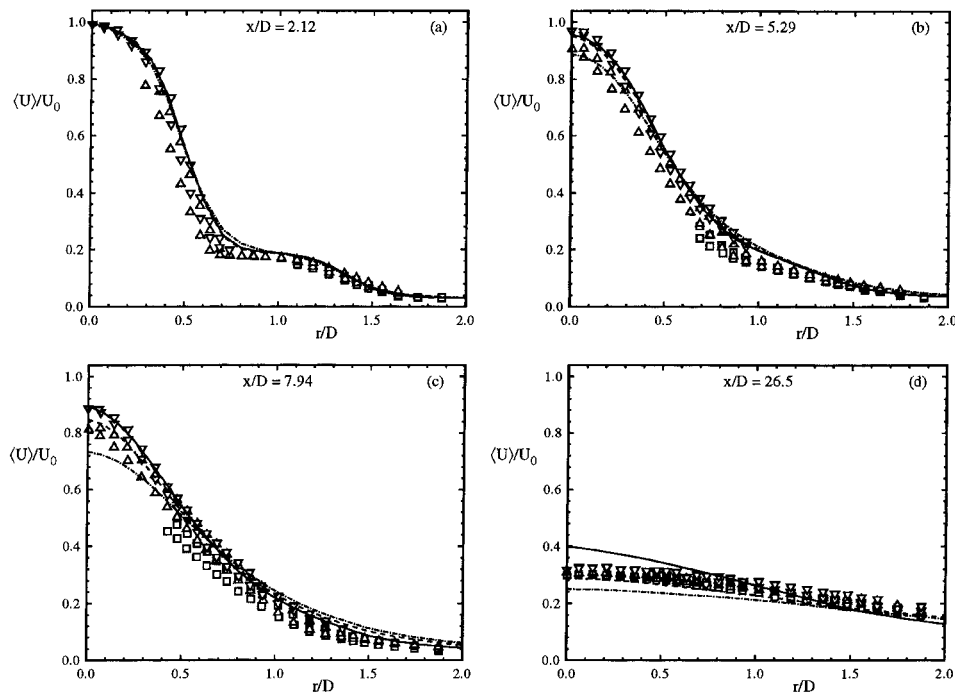


Figure 5. Predicted mean axial velocity profiles in the nonswirling co-axial jet for cases: —, W0a; - - -, L0a; and - · -, S0a; compared to experimental data of Takahashi and Vangsnes [30] with conditioning on:  $\square$ , co-flow;  $\triangle$ , annular flow; and  $\nabla$ , jet flow.

Table II. Experimental cases from Takahashi and co-workers [30, 31].

Swirl Angle	Bulk Velocity (m/s)			$U_0^1$	S
	Jet	Annulus	External		
0°	100	20	4	127.2	0.00
30°	100	20	4	131.6	0.09

<sup>1</sup>Inlet mean axial velocity measured at centerline in m/s.

The measurements were taken by a LDV technique at axial locations from  $x = 1.5$  mm ( $x/D = 0.159$ ) to  $x = 250$  mm ( $x/D = 26.5$ ) and at radial locations to  $r \sim 28$  mm ( $r/D \sim 3$ ) on either side of the centerline. The measurements across the centerline provide an indication of the experimental scatter and level of symmetry in the flow. The jet, annulus, and co-flow are seeded individually in separate experimental runs to eliminate velocity bias. The measured statistics are therefore conditioned on the origin of the fluid from which the unconditional statistics cannot be derived without additional unmeasured information. The unconditional mean

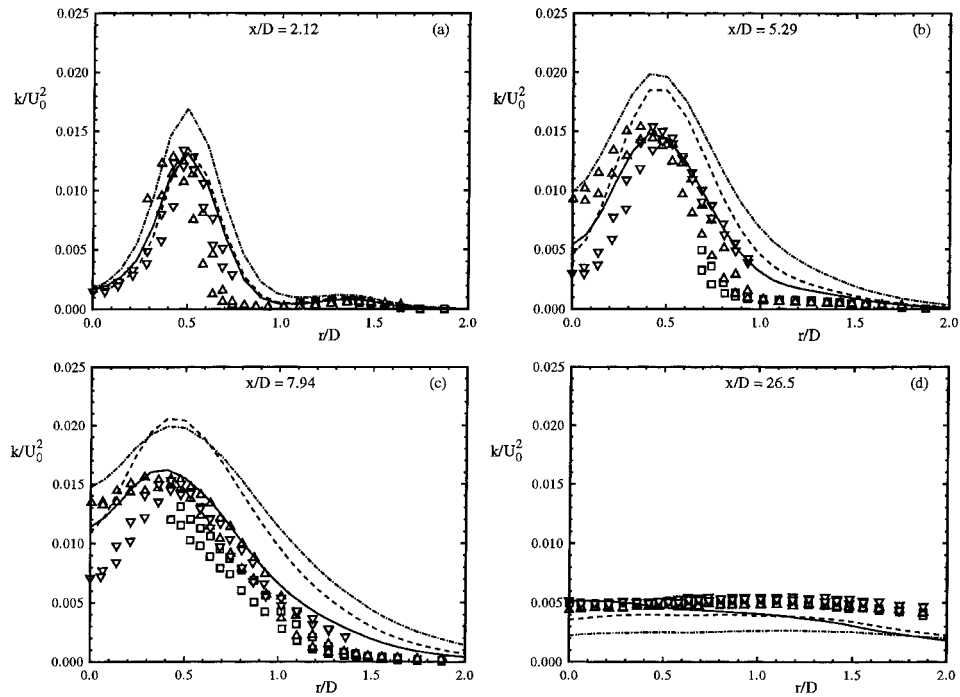


Figure 6. Predicted turbulent kinetic energy profiles in the nonswirling co-axial jet for cases: —, W0a; - - -, L0; - · -, S0a; compared to experimental data of Takahashi and Vangness [30] with conditioning on: □, co-flow; △, annular flow; and ▽, jet flow.

velocity lies within the range of the conditional means, but this is not true of the general unconditional moments (e.g., Reynolds stresses).

The conditional means can be directly evaluated in PDF methods by tagging the source of the entering particles, while in standard moment closures additional modeling assumptions are required. Representative conditional and unconditional statistics are compared in Figure 4 for the nonswirling co-axial jet at  $x/D = 5.29$ , and several observations are made. The conditional and unconditional mean axial velocities are quite similar although, as might be expected, the jet velocities are higher than the annular velocities, which in turn are higher than the co-flow velocities. In contrast, the means of the radial velocity are qualitatively different and illustrate the mixing between the streams. At further downstream locations, the jets are better mixed, and the unconditional moments tend to the moments conditioned on the co-flow due to its large mass flow rate. The unconditional Reynolds stresses are larger than the conditional Reynolds stresses across the entire layer and especially through the annular jet where fluid initiating from all three streams exists. For clarity in comparing the different models, the remaining results in this section are shown for the unconditional moments.

Table III. Simulations performed for comparisons with the experimental data of Takahashi and co-workers [30, 31].

Case Name	Swirl Angle	U* Model	$C_{pt}$	$S_\omega^1$	$C_\Omega^2$	$C_{\omega 2}/C_{\omega 1}$
<b>W0a</b>	0°	WVM	0.12	$S_\omega - P$	$C_\Omega$ -variable	1.6
<b>L0a</b>	0°	LIPM	0.2	$S_\omega - P$	$C_\Omega$ -variable	1.6
<b>S0a</b>	0°	SLM	0.0	$S_\omega - P$	$C_\Omega$ -variable	1.6
<b>W30a</b>	30°	WVM	0.12	$S_\omega - P$	$C_\Omega$ -variable	1.6
W30b	30°	WVM	0.12	$S_\omega - P$	$C_\Omega$ -variable	1.8
W30c	30°	WVM	0.12	$S_\omega - P$	$C_\Omega$ -fixed	1.6
W30d	30°	WVM	0.0	$S_\omega - P$	$C_\Omega$ -variable	1.6
W30e	30°	WVM	0.12	$S_\omega - S$	$C_\Omega$ -fixed	1.6 <sup>3</sup>
W30f	30°	WVM	0.12	$S_\omega - S$	$C_\Omega$ -fixed	2.7 <sup>3</sup>
<b>L30a</b>	30°	LIPM	0.2	$S_\omega - P$	$C_\Omega$ -variable	1.6
L30b	30°	LIPM	0.2	$S_\omega - P$	$C_\Omega$ -variable	1.8
L30c	30°	LIPM	0.2	$S_\omega - P$	$C_\Omega$ -variable	1.3
L30d	30°	LIPM	0.2	$S_\omega - S$	$C_\Omega$ -fixed	2.0 <sup>3</sup>
<b>S30a</b>	30°	SLM	0.0	$S_\omega - P$	$C_\Omega$ -variable	1.6

<sup>1</sup>The notation  $S_\omega - P$  refers to the model of Equation (16), while  $S_\omega - S$  refers to that of Equation (17).

<sup>2</sup>The notation  $C_\Omega$ -variable refers to the variable form of the coefficient in Equation (15), while  $C_\Omega$ -fixed refers to  $C_\Omega = 0.6893$ .

<sup>3</sup>Assumes  $C_\mu = 0.09$ .

In the PDF calculations, the geometry is assumed to be axisymmetric with an outer radius,  $R_c = 75$  mm. Inlet conditions for the mean velocity and Reynolds stresses are specified from the experimental data at the initial axial location,  $x/D = 0.159$ . An equilibrium assumption (i.e.,  $S_\omega = 0.0$  or  $P/\varepsilon = C_{\omega 2}/C_{\omega 1}$ ) is made for the inlet mean turbulent frequency,  $\langle \omega \rangle_I$ , which gives

$$\langle \omega \rangle_I = -\frac{2C_{\omega 1}}{C_{\omega 2}} b_{ij} S_{ij}. \quad (20)$$

The simulations are performed on a  $36 \times 36$  nonuniform grid with an initial 400 particles per cell and are run to a statistically stationary state where time averaging is then performed.

The specifics of the cases studied are provided in Table III. Each bold-faced case name represents a base set of models for each type of particle velocity model. The base set of models includes the pressure transport model for the LIPM and WVM (not SLM) and the turbulent frequency model with the production-to-dissipation form of  $S_\omega$  ( $S_\omega - P$ ), and the variable form of  $C_\Omega$  ( $C_\Omega$ -variable). Finally, the model parameters for the base models are provided in Table I.

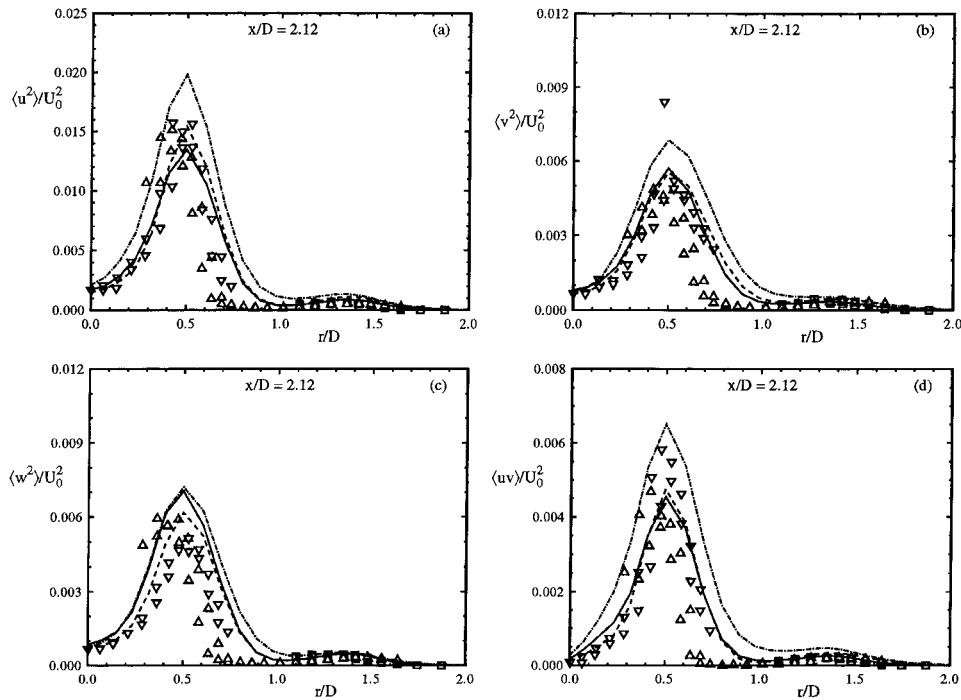


Figure 7. Predicted Reynolds stress profiles in the nonswirling co-axial jet: (a)  $\langle u^2 \rangle$ ; (b)  $\langle v^2 \rangle$ ; (c)  $\langle w^2 \rangle$ ; and (d)  $\langle uv \rangle$ ; at  $x/D = 2.12$  for cases: —, W0a; - - -, L0a; and - · - ·, S0a; compared to experimental data of Takahashi and Vangsnes [30] with conditioning on:  $\square$ , co-flow;  $\triangle$ , annular flow; and  $\nabla$ , jet flow.

### 3.1.1. Calculation of nonswirling jet

The performance of the velocity models is examined through comparisons with the experimental data for the nonswirling co-axial jet. Mean axial velocity profiles are illustrated at several axial locations in Figure 5. The models all agree with the experimental data quite well, but the LIPM (- - - lines) matches the centerline velocity at large axial distances better than the SLM (- · - · lines) and the WVM (— lines). The unconditional kinetic energy profile from the WVM compares very well with the conditional experimental data in Figure 6 for all axial locations, but the WVM slightly under-predicts the conditional kinetic energy (not shown) at  $x/D = 5.29$ . The LIPM and SLM predict the conditional kinetic energy at  $x/D = 5.29$  very well, but over-predict it at  $x/D = 7.94$ . The SLM tends to spread the energy quicker than the other models, which is related to the decay of the centerline mean axial velocity. Similar conclusions are reached for the individual Reynolds normal stresses in Figures 7–9.

With respect to the evolution of the nonswirling flow, the Reynolds shear stress  $\langle uv \rangle$  dominates the effects of the other Reynolds stresses and is chiefly responsible for the spreading of the jets. The profiles of the shear stress are also shown in

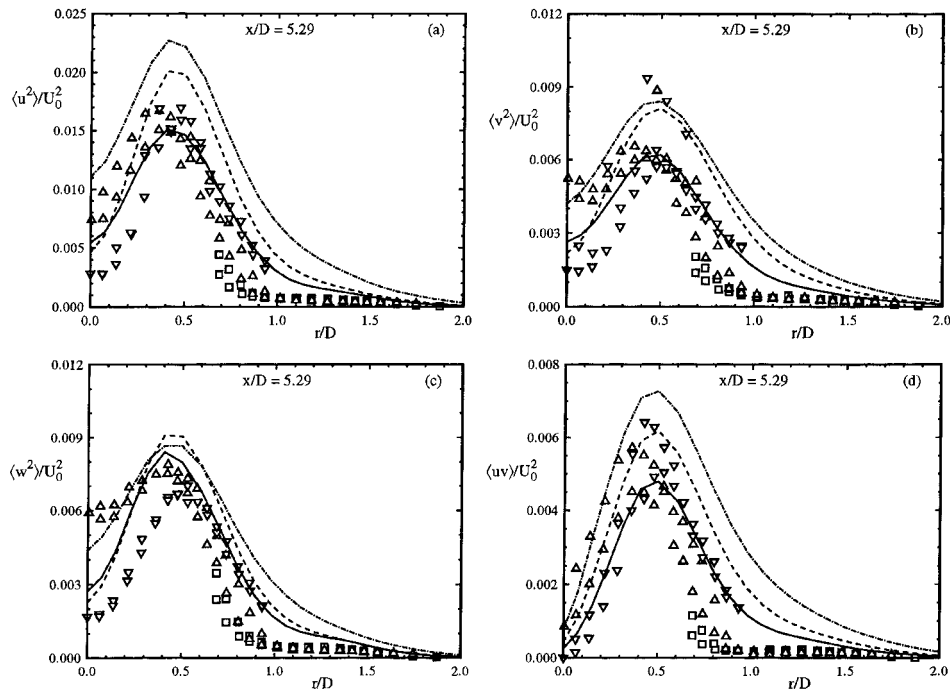


Figure 8. Predicted Reynolds stress profiles in the nonswirling co-axial jet: (a)  $\langle u^2 \rangle$ ; (b)  $\langle v^2 \rangle$ ; (c)  $\langle w^2 \rangle$ ; and (d)  $\langle uv \rangle$ ; at  $x/D = 5.29$  for cases: —, W0a; - - -, L0a; and - · - ·, S0a; compared to experimental data of Takahashi and Vangsnes [30] with conditioning on:  $\square$ , co-flow;  $\Delta$ , annular flow; and  $\nabla$ , jet flow.

Figures 7–9. At  $x/D = 5.29$ , the LIPM matches the shear stress very well. The WVM predicts slightly low values at this location, while the SLM predicts slightly high values. The differences in the shear stresses are observable in the axial mean velocity profiles at locations further downstream (i.e., the centerline mean axial velocity decays too slowly in the WVM and too quickly in the SLM).

The evolution of the mean velocity profiles for the nonswirling co-axial jets simulated are fairly insensitive to the velocity model, but are sensitive to the parameters in the turbulent frequency model. The turbulent frequency model has a large impact on the kinetic energy through its control of the dissipation. The Reynolds stress anisotropies are normalized by the kinetic energy and form a better test of the velocity models. The Reynolds stress anisotropy profiles at  $x/D = 5.29$  are presented in Figure 10. The figure illustrates that the WVM performs better than the SLM and LIPM, despite the better predictions of the mean velocity profiles from the LIPM. This issue is addressed further with regards to the swirling co-axial jets.

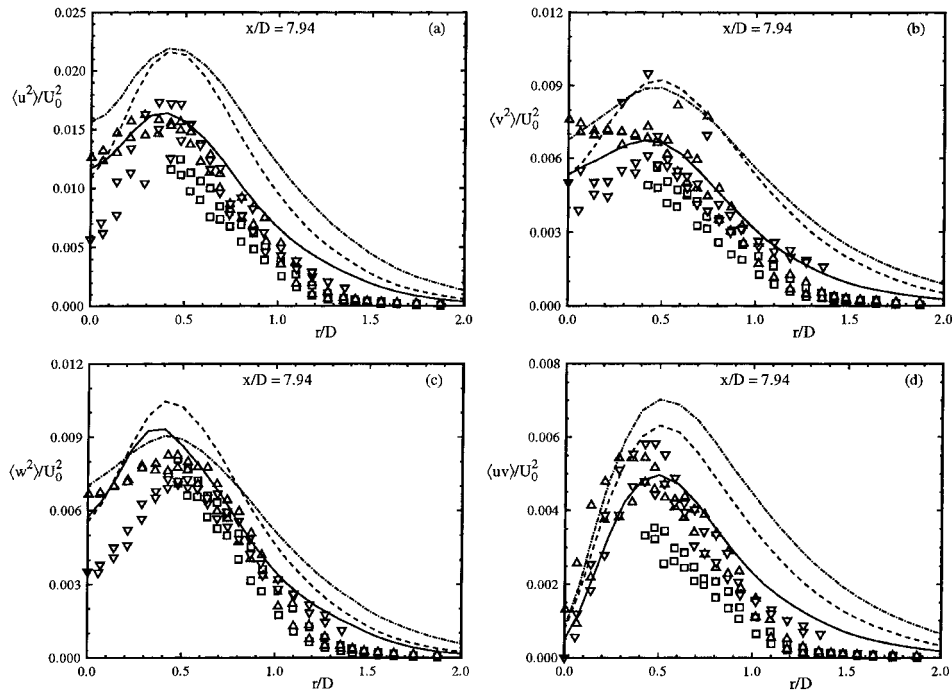


Figure 9. Predicted Reynolds stress profiles in the nonswirling co-axial jet: (a)  $\langle u^2 \rangle$ ; (b)  $\langle v^2 \rangle$ ; (c)  $\langle w^2 \rangle$ ; and (d)  $\langle uv \rangle$ ; at  $x/D = 7.94$  for cases: —, W0a; - - -, L0a; and - · - ·, S0a; compared to experimental data of Takahashi and Vangsnes [30] with conditioning on:  $\square$ , co-flow;  $\triangle$ , annular flow; and  $\nabla$ , jet flow.

### 3.1.2. Calculation of swirling jet

The performance of the velocity models is examined through comparisons with the experimental data for the swirling co-axial jet. The base models in cases W30a, L30a, and S30a are examined first. The mean axial and tangential velocity profiles are presented at several axial locations in Figures 11 and 12, while the kinetic energy and Reynolds stresses are presented in Figures 13–16.

The conclusions for the mean axial velocity are similar to those from the nonswirling case. In Figure 11, the LIPM (— lines) matches the decay of the centerline velocity slightly better than both the WVM (— lines) which decays too slowly and the SLM (--- lines) which decays too rapidly. The LIPM and WVM predict the spreading of the mean tangential velocity very well in Figure 12, while the peak value decays too rapidly in the SLM.

The swirl number is quite low in this flow, and the axial-radial Reynolds shear stress,  $\langle uv \rangle$ , dominates the effects of the swirl in the evolution of the mean axial velocity. The radial-tangential Reynolds shear stress,  $\langle vw \rangle$ , plays a similar role in the evolution of the mean tangential velocity as does  $\langle uv \rangle$  in the evolution of the mean axial velocity. In Figure 14, the SLM over-predicts the peaks of  $\langle uv \rangle$  and

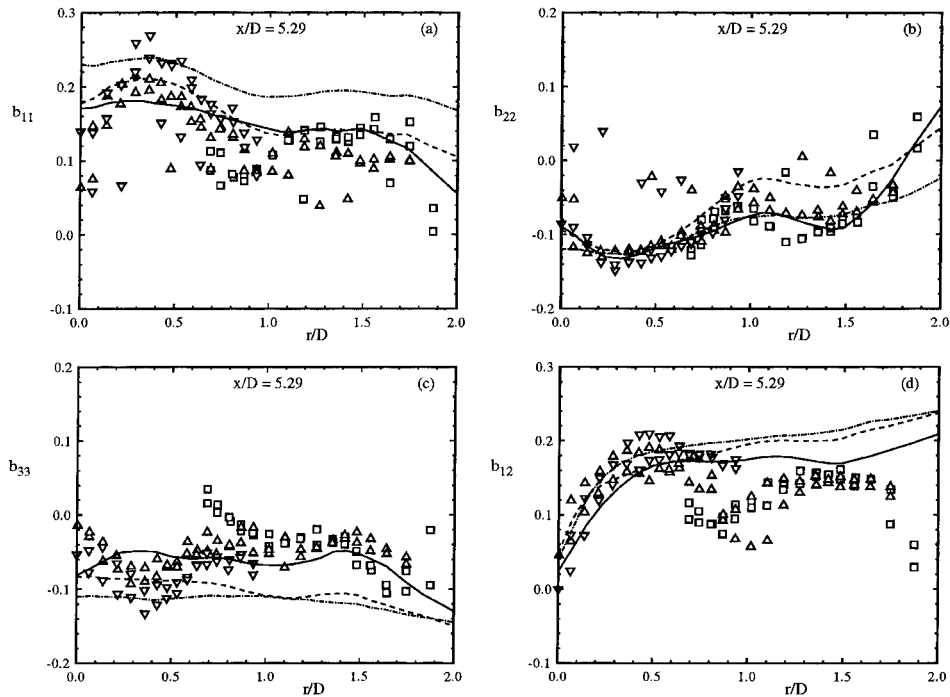


Figure 10. Predicted Reynolds stress anisotropy profiles in the nonswirling co-axial jet: (a)  $b_{11}$ ; (b)  $b_{22}$ ; (c)  $b_{33}$ ; and (d)  $b_{12}$ ; at  $x/D = 5.29$  for cases: —, W0a; - - -, LOa; and - · -, S0a; compared to experimental data of Takahashi and Vangsnæs [30] with conditioning on:  $\square$ , co-flow;  $\triangle$ , annular flow; and  $\nabla$ , jet flow.

$\langle vw \rangle$  at  $x/D = 2.65$  producing the too rapid decay in the mean axial and tangential velocities. The WVM and LIPM provide lower peaks for these shear stresses and match the experimental data better. As in the nonswirling case, the LIPM predicts larger kinetic energies and Reynolds normal stresses than does the WVM, but smaller values than the SLM. All three models still match the experimental data quite well for these quantities given the scatter in the data. The axial-tangential shear stress,  $\langle uw \rangle$ , is of minor importance to the evolution of the mean velocities, and the experimental data for this statistic contains significant scatter.

The Reynolds stress anisotropies are shown in Figures 17–19. Again, the WVM predicts the experimental data for the anisotropies slightly better than the LIPM and SLM, although the differences between the velocity models is smaller for the anisotropies than for the kinetic energies. The effects of the velocity models appear quite minor and are illustrated to be secondary to the specification of turbulent frequency model parameters in the following section.

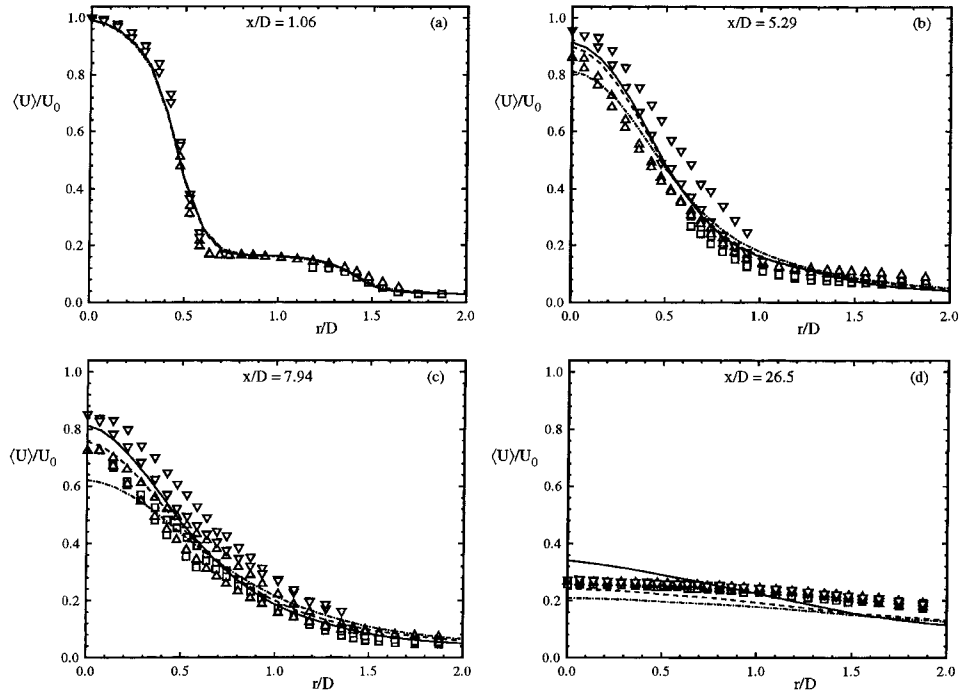


Figure 11. Predicted mean axial velocity profiles in the swirling co-axial jet for cases: —, W30a; - - -, L30a; and ---, S30a; compared to experimental data of Takahashi et al. [31] with conditioning on: □, co-flow; △, annular flow; and ▽, jet flow.

### 3.1.3. Sensitivity to frequency model

The WVM and LIPM base models which include the revised turbulent frequency model give good agreement in both the nonswirling co-axial jet (cases W0a and L0a) and the swirling co-axial jet (cases W30a and L30a). The turbulent frequency plays a crucial role in the evolution of the jets through its description of the dissipation. A closer examination of the turbulent frequency model is achieved by individually studying the effects of the revisions to the original model. Simulations with the LIPM and WVM are performed in the swirling co-axial jet, as detailed in Table III, with the production-to-dissipation ( $S_\omega - P$ ) and mean strain-rate-squared ( $S_\omega - S$ ) source of turbulent frequency models and with the constant and variable form of  $C_\Omega$  models. The centerline mean axial velocity is a sensitive measure of a jet's spreading, and in Figure 20 this velocity is shown for the WVM and LIPM cases. The important conclusions from this figure are listed below.

1. The base models (W30a and L30a) give reasonable agreement (less than 20% error for the WVM and 13% error for the LIPM) with the experimental data for the centerline mean axial velocity.

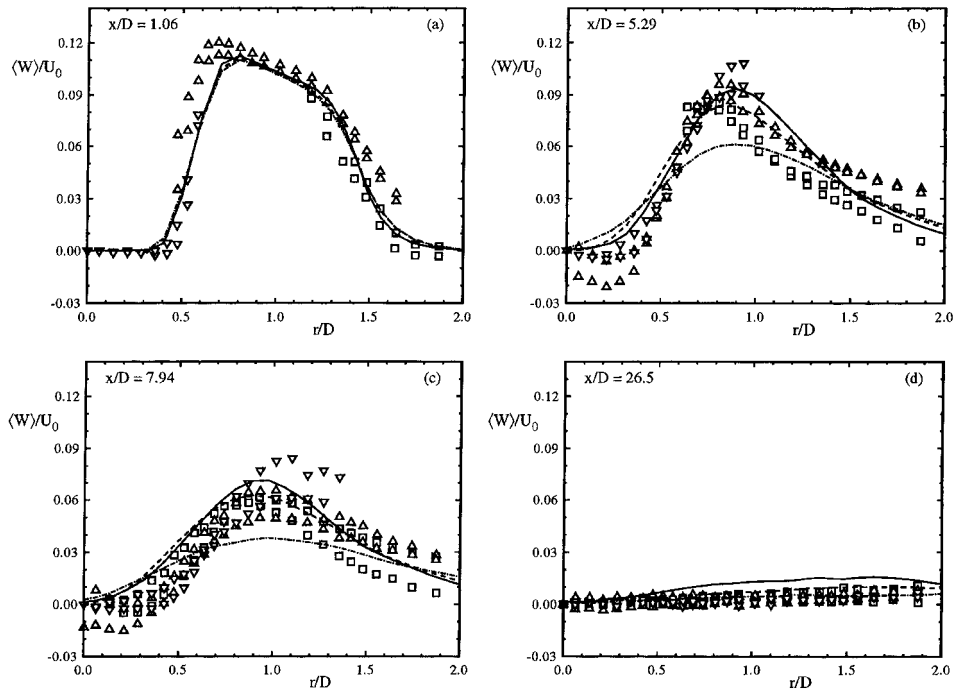


Figure 12. Predicted mean tangential velocity profiles in the swirling co-axial jet for cases: —, W30a; - - -, L30a; and - · - ·, S30a; compared to experimental data of Takahashi et al. [31] with conditioning on:  $\square$ , co-flow;  $\triangle$ , annular flow; and  $\nabla$ , jet flow.

2. The variable form of  $C_\Omega$  (Equation (15)), which is part of the revised turbulent frequency model in the base model (case W30a, — lines), has a very small effect relative to  $C_\Omega = 0.6893$  from case W30c (-·-· lines) for this flow.
3. Increasing the ratio  $C_{\omega 2}/C_{\omega 1}$  by decreasing  $C_{\omega 1}$  for a fixed  $C_{\omega 2} = 0.9$  (i.e., increasing  $(P/\varepsilon)_\infty$ ) increases the spreading rate of the jets, which increases the decay of the centerline mean axial velocity. The simulations are sensitive to this parameter ratio.
4. Comparable results can be obtained with the original source of turbulent frequency model, but with larger values of the ratio  $C_{\omega 2}/C_{\omega 1}$ . The case W30f (-·-· line in Figure 20a) with  $C_{\omega 2}/C_{\omega 1} = 2.7$  and the case L30c (-·-· line in Figure 20b) with  $C_{\omega 2}/C_{\omega 1} = 2.0$  are comparable to the WVM and LIPM base models, respectively.

The profiles for the axial-radial Reynolds shear stress  $\langle uv \rangle$ , the production-to-dissipation of turbulent kinetic energy ratio  $P/\varepsilon$ , the turbulent kinetic energy  $k$ , and the conditional-mean turbulent frequency  $\Omega$  from the WVM cases are presented at  $x/D = 7.94$  in Figure 21, and the corresponding plots for the LIPM cases are

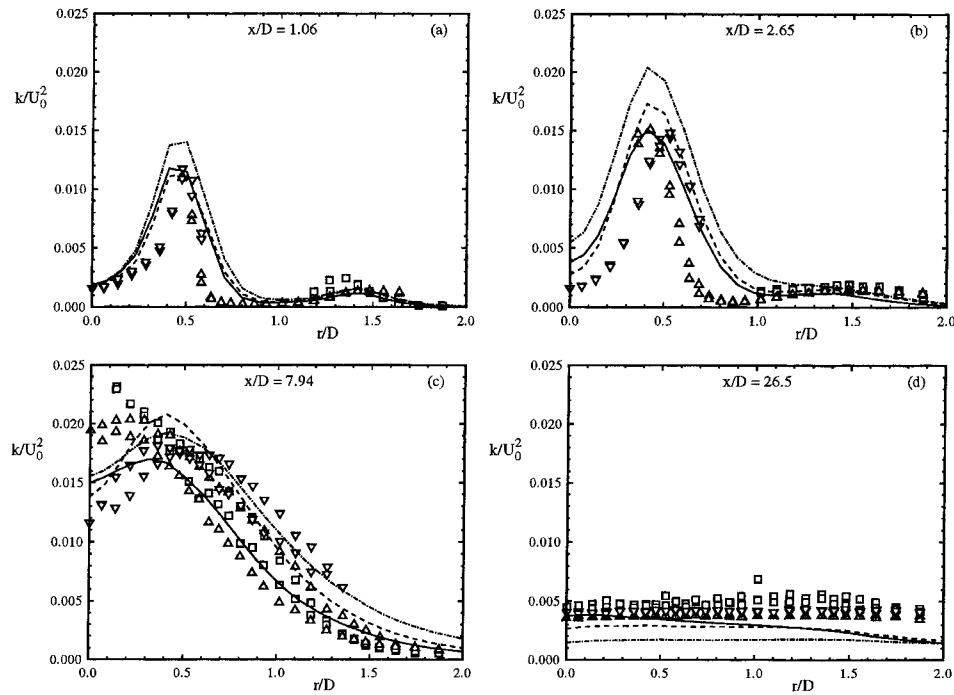


Figure 13. Predicted turbulent kinetic energy profiles in swirling the co-axial jet for cases: —, W30a; - - -, L30a; and ---, S30a; compared to experimental data of Takahashi et al. [31] with conditioning on: □, co-flow; △, annular flow; and ▽, jet flow.

contained in Figure 22. These figures further illustrate the conclusions expressed for the decay of the centerline mean axial velocity.

The ratio  $C_{\omega 2}/C_{\omega 1}$  maintains a strong influence on the evolution of the flow. An increased  $C_{\omega 2}/C_{\omega 1}$  provides a larger  $P/\varepsilon$  ratio (Figures 21b and 22b) throughout the flow, which yields an increased turbulent kinetic energy (Figures 21c and 22c) and a decreased dissipation. The conditional-mean turbulent frequency (Figures 21d and 22d) is thereby decreased. The velocity models chiefly influence the Reynolds stress anisotropy, so an increased kinetic energy with a fixed anisotropy yields an increased Reynolds shear stress (Figures 21a and 22a). The increased shear stress results in a faster spreading rate in the jets, which is the crucial factor in correctly modeling the mean velocity profiles. The sensitivity of the spreading rate to the parameters in the modeled source of turbulent frequency makes detailed comparisons between velocity models very difficult.

For the model parameters selected, the original turbulent frequency model provides comparable results to the revised model in Figures 21 and 22. The parameter ratio  $C_{\omega 2}/C_{\omega 1}$  does not fully describe the  $P/\varepsilon$  ratio due to turbulent transport, but in the revised model the parameter ratio does provide an estimate for the peak values in the  $P/\varepsilon$  ratio profiles. In the original turbulent frequency model,

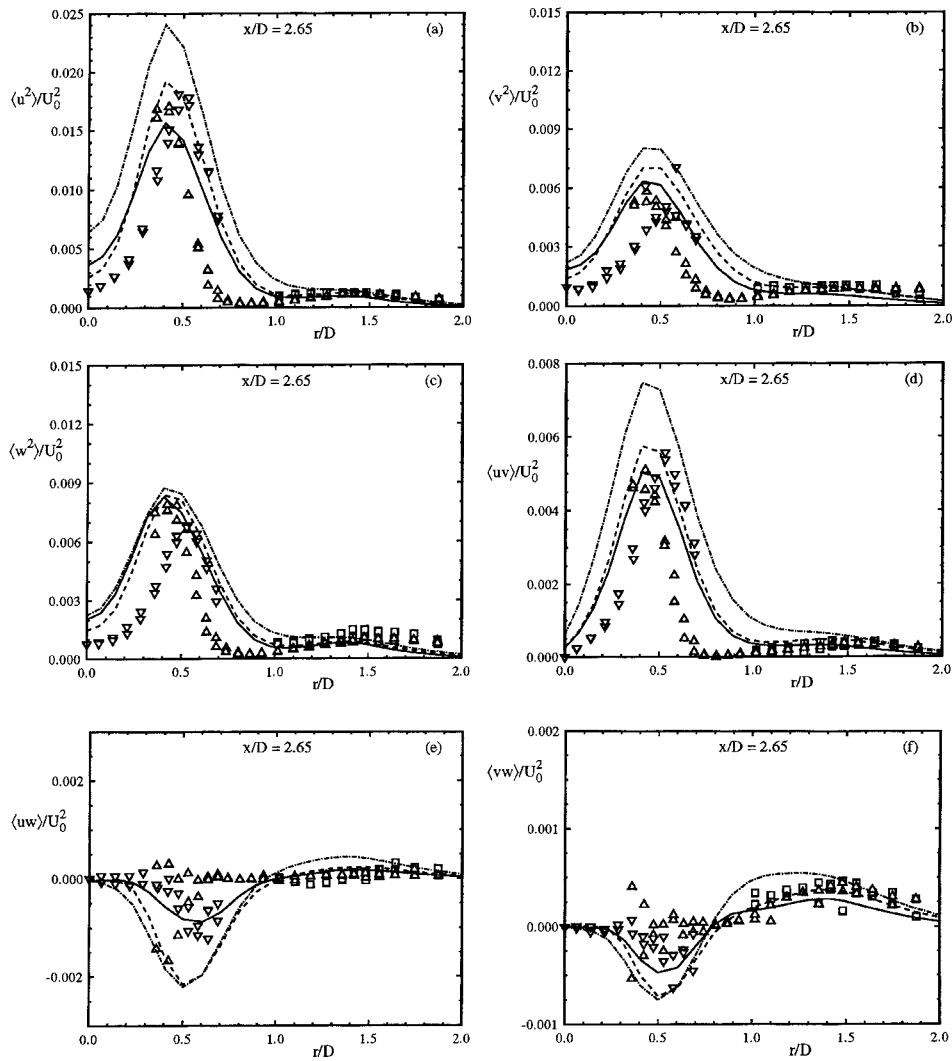


Figure 14. Predicted Reynolds stress profiles in the swirling co-axial jet: (a)  $\langle u^2 \rangle$ ; (b)  $\langle v^2 \rangle$ ; (c)  $\langle w^2 \rangle$ ; (d)  $\langle uv \rangle$ ; (e)  $\langle uw \rangle$ ; and (f)  $\langle vw \rangle$ ; at  $x/D = 2.65$  for cases: —, W30a; - - -, L30a; and - · - ·, S30a; compared to experimental data of Takahashi et al. [31] with conditioning on:  $\square$ , co-flow;  $\triangle$ , annular flow; and  $\nabla$ , jet flow.

the gradient transport parameter  $C_\mu$  must be specified to calculate the parameter ratio. With the standard  $k$ - $\varepsilon$  specification of  $C_\mu = 0.09$ , the parameter ratios are much larger than the calculated  $P/\varepsilon$  ratio. This indicates that the value of  $C_\mu$  may be too large for this flow and shows that direct comparisons of the parameter ratio between the original and revised models are not appropriate.

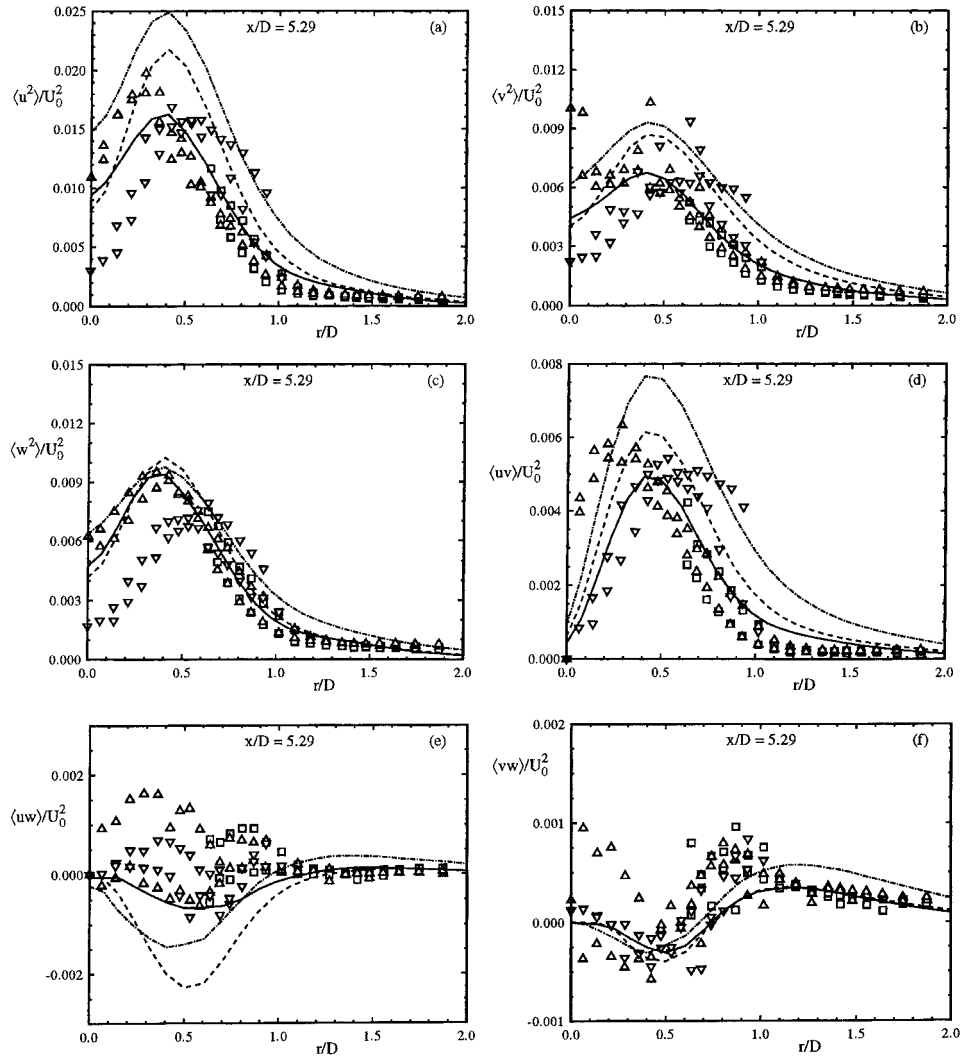


Figure 15. Predicted Reynolds stress profiles in the swirling co-axial jet: (a)  $\langle u^2 \rangle$ ; (b)  $\langle v^2 \rangle$ ; (c)  $\langle w^2 \rangle$ ; (d)  $\langle uv \rangle$ ; (e)  $\langle uw \rangle$ ; and (f)  $\langle vw \rangle$ ; at  $x/D = 5.29$  for cases: —, W30a; - - -, L30a; and - · - ·, S30a, compared to experimental data of Takahashi et al. [31] with conditioning on:  $\square$ , co-flow;  $\triangle$ , annular flow; and  $\nabla$ , jet flow.

Finally, the normalized variance of turbulent frequency (not shown) is typically larger than 0.25 and the conditional-mean turbulent frequency is lower using the variable form of  $C_\Omega$ . However, the impact of the change in  $C_\Omega$  is relatively minor for the evolution of the flow, as is illustrated in Figures 21 and 22 by comparing case W30a (— lines) to case W30c (--- lines).

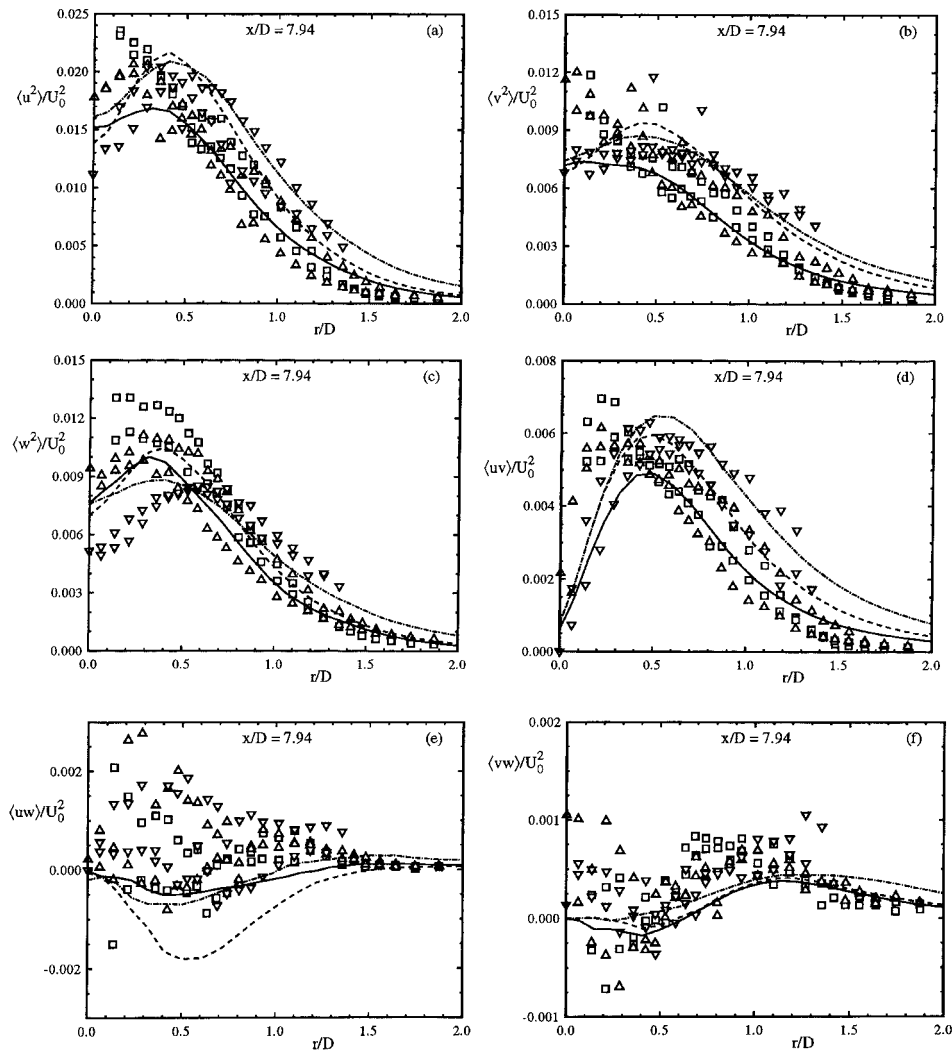


Figure 16. Predicted Reynolds stress profiles in the swirling co-axial jet: (a)  $\langle u^2 \rangle$ ; (b)  $\langle v^2 \rangle$ ; (c)  $\langle w^2 \rangle$ ; (d)  $\langle uv \rangle$ ; (e)  $\langle uw \rangle$ ; and (f)  $\langle vw \rangle$ ; at  $x/D = 7.94$  for cases: —, W30a; - - -, L30a; and - · - ·, S30a; compared to experimental data of Takahashi et al. [31] with conditioning on:  $\square$ , co-flow;  $\triangle$ , annular flow; and  $\nabla$ , jet flow.

#### 3.1.4. Sensitivity to pressure transport model

The effects of the pressure transport model are also secondary to the turbulence frequency modeling in the evolution of the swirling co-axial jet. The pressure transport model acts to push energetic particles up the kinetic energy gradient. Since the radial gradients are much larger than axial gradients, the model has the greatest impact on the radial-radial and axial-radial Reynolds stresses,  $\langle v^2 \rangle$  and  $\langle uv \rangle$ . The

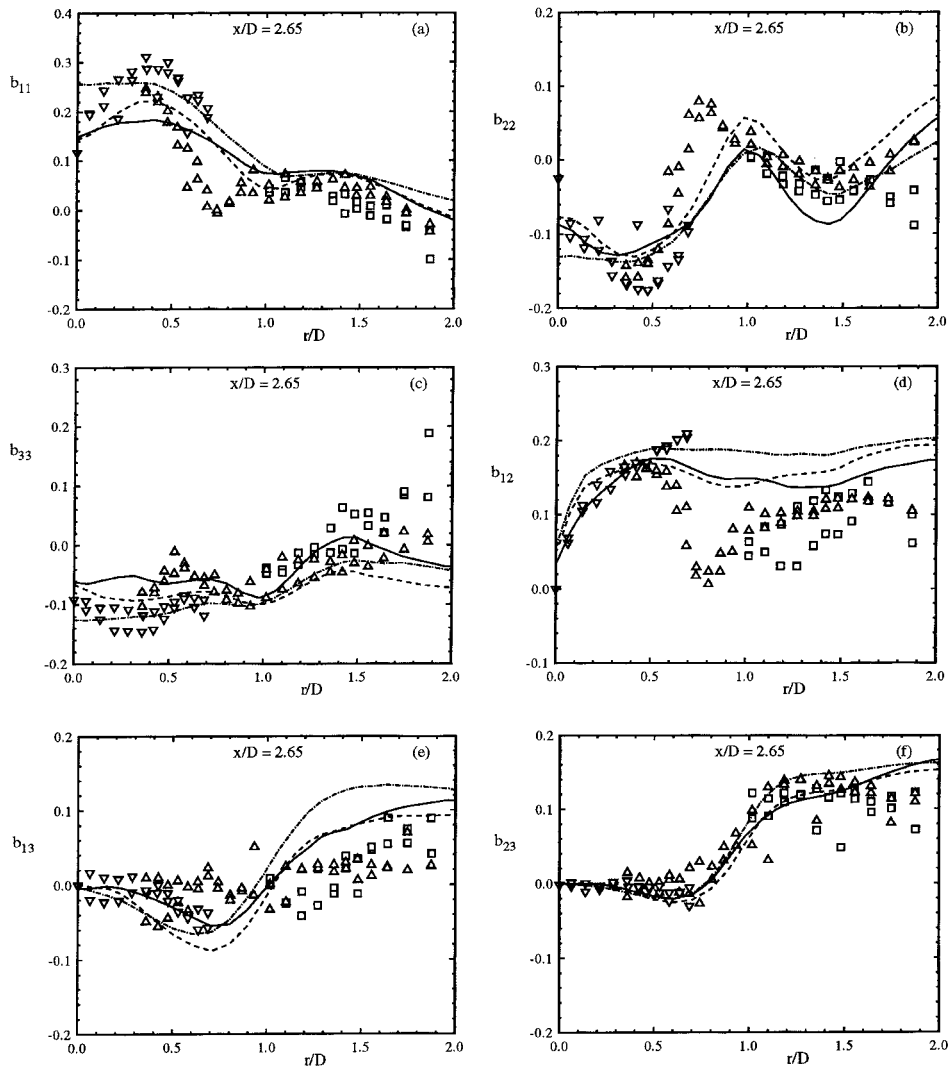


Figure 17. Predicted Reynolds stress anisotropy profiles in the swirling co-axial jet: (a)  $b_{11}$ ; (b)  $b_{22}$ ; (c)  $b_{33}$ ; (d)  $b_{12}$ ; (e)  $b_{13}$ ; and (f)  $b_{23}$ ; at  $x/D = 2.65$  for cases: —, W30a; - - -, L30a; and - · - ·, S30a; compared to experimental data of Takahashi et al. [31] with conditioning on: □, co-flow; △, annular flow; and ▽, jet flow.

kinetic energy, conditional-mean turbulent frequency, and these Reynolds stress profiles are provided at  $x/D = 7.94$  in Figure 23. It may be seen that the main effect of the pressure transport model is to reduce the Reynolds stresses at the edge of the jet. The pressure transport model acts as an added anisotropic dissipation in regions of large kinetic energy gradients. From the anisotropy profiles, the model tends to improve the results for larger  $r/D$ . The mean velocities, however, show

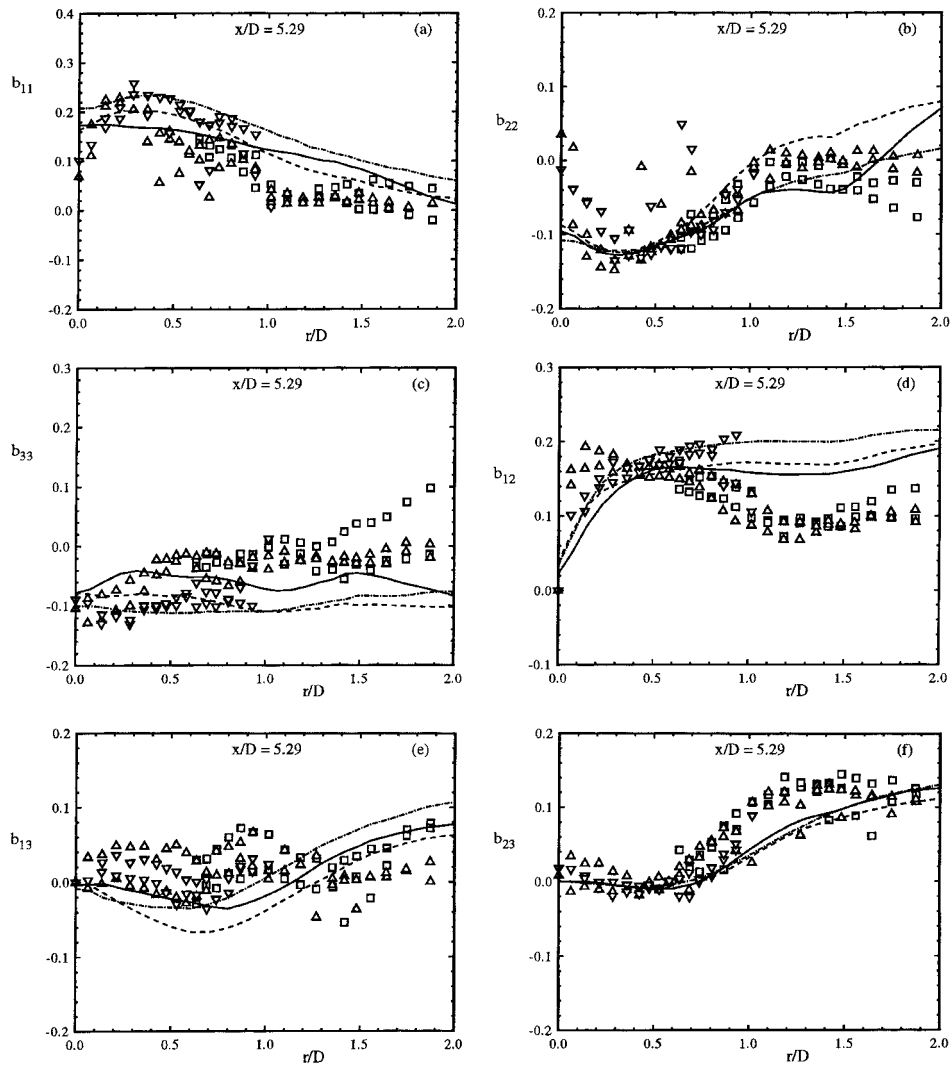


Figure 18. Predicted Reynolds stress anisotropy profiles in the swirling co-axial jet: (a)  $b_{11}$ ; (b)  $b_{22}$ ; (c)  $b_{33}$ ; (d)  $b_{12}$ ; (e)  $b_{13}$ ; and (f)  $b_{23}$ ; at  $x/D = 5.29$  for cases: —, W30a; - - -, L30a; and - · -, S30a; compared to experimental data of Takahashi et al. [31] with conditioning on:  $\square$ , co-flow;  $\triangle$ , annular flow; and  $\nabla$ , jet flow.

little effect of the pressure transport modeling in contrast to the results previously demonstrated for the temporal shear layer [2].

### 3.2. TEMPORAL SHEAR LAYER

The temporal shear layer is a statistically one-dimensional, turbulent layer that grows between two semi-infinite nonturbulent streams of equal and opposite velo-

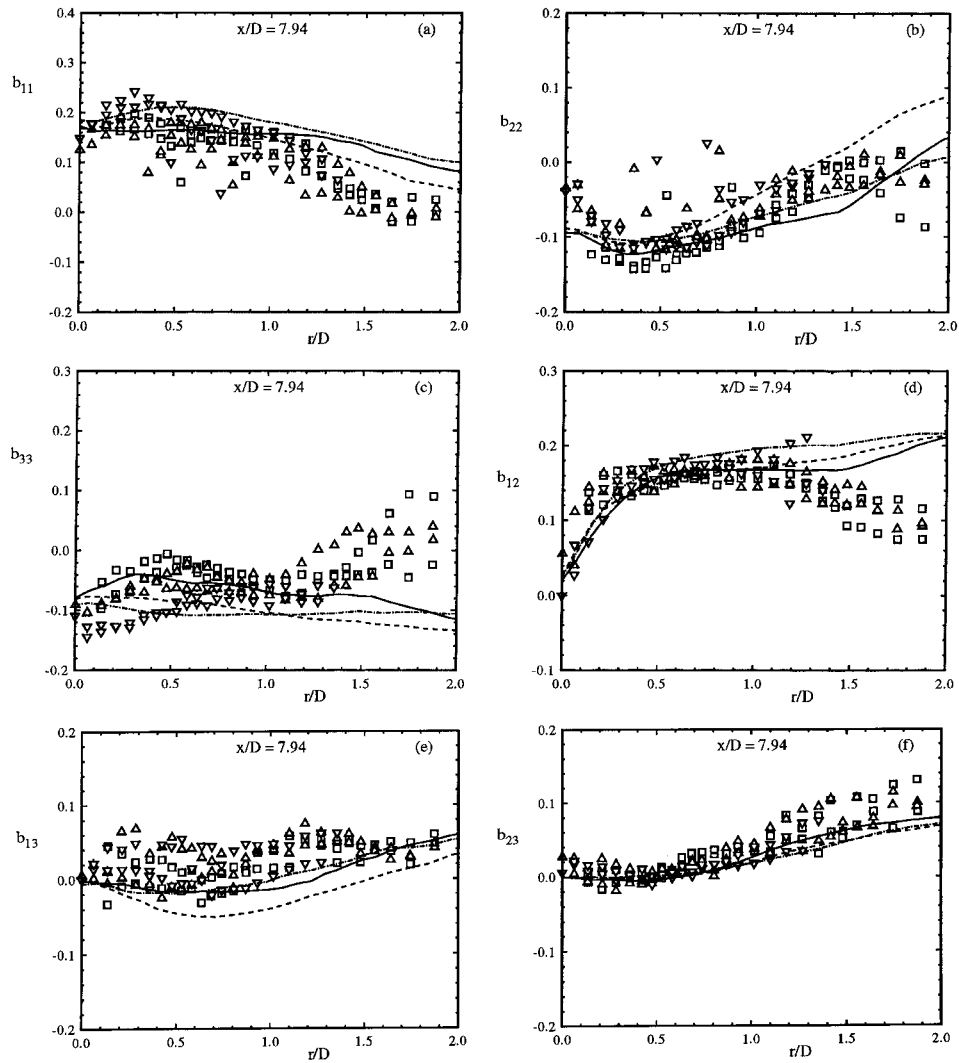


Figure 19. Predicted Reynolds stress anisotropy profiles in the swirling co-axial jet: (a)  $b_{11}$ ; (b)  $b_{22}$ ; (c)  $b_{33}$ ; (d)  $b_{12}$ ; (e)  $b_{13}$ ; and (f)  $b_{23}$ ; at  $x/D = 7.94$  for cases: —, W30a; - - -, L30a; and - · -, S30a; compared to experimental data of Takahashi et al. [31] with conditioning on: □, co-flow; △, annular flow; and ▽, jet flow.

city. It is the limiting case of the plane (spatial) mixing layer as the velocity ratio approaches one. The velocity difference between the two streams,  $\Delta U$ , and the momentum thickness of the layer,  $\delta_m$ , are the characteristic velocity and length scales which are used to construct a self-similar solution. The layer growth rate,

$$r \equiv \frac{1}{\Delta U} \frac{d\delta_m}{dt}, \quad (21)$$

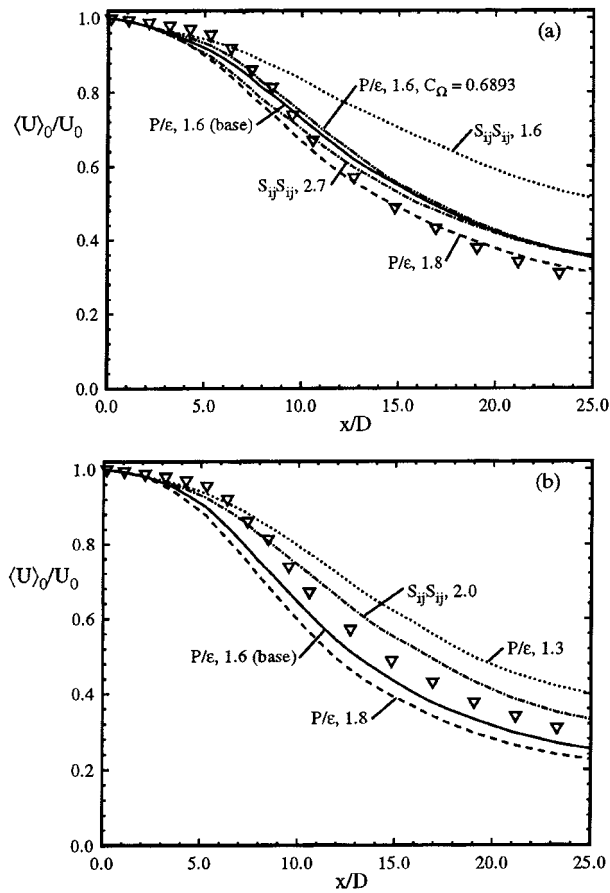


Figure 20. Predicted center line mean velocity in the swirling co-axial jet for (a) WVM cases: —, W30a; ---, W30b; - - - W30c; · · ·, W30e; and - - -, W30f; and (b) LIPM cases: —, L30a; - - -, L30b; · · ·, L30c; - - -, L30d; and compared to experimental data of Takahashi et al. [31]  $\nabla$  with conditioning on the jet flow.

is a constant in the similarity equations.

The revised form of the turbulent frequency model from Section 2.3 and the original model from Jayesh and Pope [27] are combined with the WVM and the pressure transport model and applied to the temporal shear layer. The results are compared to the DNS data of Rogers and Moser [23] in a temporal shear layer and the experimental data of Bell and Mehta [32] in a plane mixing layer. A detailed study of the different velocity models is performed in [2], and temporal shear layer results are included here to illustrate the robust nature of the turbulent frequency model. The cases studied are given in Table IV.

The calculated values of the growth rate compare well with the DNS and experimental data in cases TSa, TSb, TSc and TSe (see Table IV), but the growth rate is a relatively weak measure of the turbulence model's performance. In Figure 24,

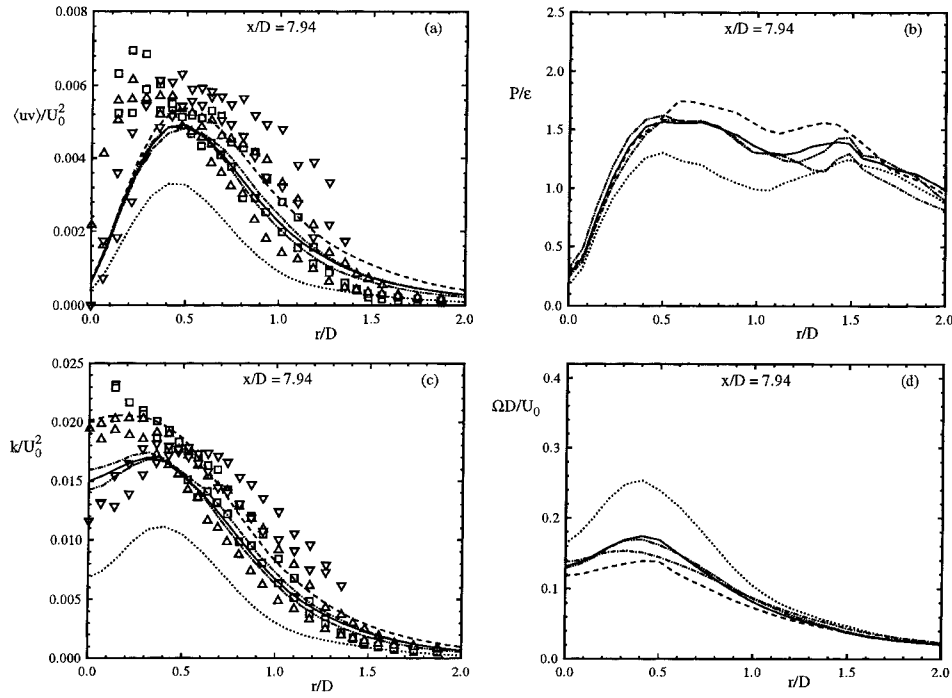


Figure 21. Predictions of the WVM in the swirling co-axial jet at  $x/D = 7.94$  for: (a)  $\langle uv \rangle$ ; (b)  $P/\epsilon$ ; (c)  $k$ ; and (d)  $\Omega$ ; in cases: —, W30a; - - -, W30b; ····, W30c; ····, W30e; and ····, W30f; compared to experimental data of Takahashi et al. [31] with conditioning on:  $\square$ , co-flow;  $\triangle$ , annular flow; and  $\nabla$ , jet flow.

Table IV. Directory of test cases run for the temporal shear layer with their growth rates.

Case	$S_\omega$	$C_\Omega$	$C_{\omega 2}/C_{\omega 1}$	$(P/\epsilon)_c^1$	$r$
TSa	$S_\omega - P$	$C_\Omega$ -variable	1.6	1.63	0.014
TSb	$S_\omega - P$	$C_\Omega$ -variable	1.5	1.57	0.014
TSd	$S_\omega - P$	$C_\Omega$ -fixed	1.6	1.65	0.014
TSd	$S_\omega - S$	$C_\Omega$ -fixed	$1.6^2$	1.21	0.008
TSe <sup>3</sup>	$S_\omega - S$	$C_\Omega$ -fixed	$2.76^2$	1.49	0.013
DNS <sup>4</sup>	—	—	—	1.47	0.014
Experimental Range <sup>5</sup>	—	—	—	—	0.014–0.022

<sup>1</sup>Calculated production-to-dissipation ratio averaged over central region,  $|\xi| \leq 2.0$ .

<sup>2</sup>Assumes  $C_\mu = 0.09$ .

<sup>3</sup>Case studied in Van Slooten et al. [2].

<sup>4</sup>Direct numerical simulation of Rogers and Moser [23].

<sup>5</sup>Taken from calculations by Rogers and Moser [23] of data in Dimotakis [45].

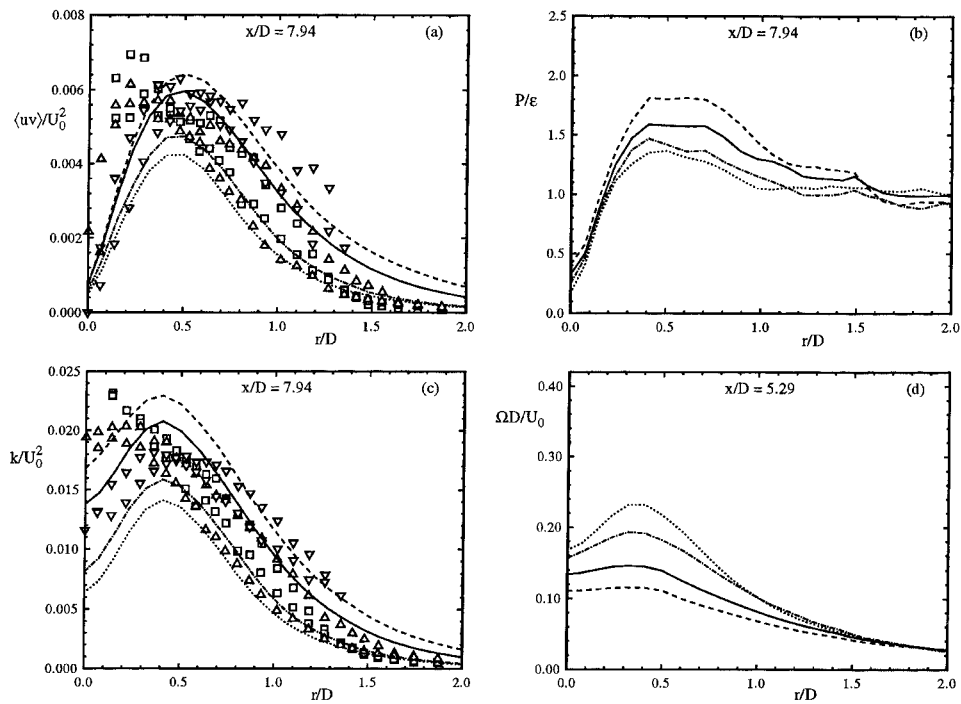


Figure 22. Predictions of the LIPM in the swirling co-axial jet at  $x/D = 7.94$  for: (a)  $\langle uv \rangle$ ; (b)  $P/\epsilon$ ; (c)  $k$ ; and (d)  $\Omega$ ; in cases: —, L30a; ---, L30b; ···, L30c; -·-, L30d; and compared to experimental data of Takahashi et al. [31] with conditioning on:  $\square$ , co-flow;  $\triangle$ , annular flow; and  $\nabla$ , jet flow.

the DNS and experimental data for the mean velocity profiles are predicted very well in all cases, but also show little influence of the different turbulent frequency models. This is in direct contrast to the co-axial jets in Section 3.1 where the ratio  $C_{\omega 2}/C_{\omega 1}$  has a very strong influence on the spatial evolution of the flow. From [2], the pressure transport model greatly affects the mean velocity by increasing the gradient of the Reynolds shear stress near the edge of the layer. This is another difference from the conclusions of the co-axial jets, where the pressure transport has a negligible effect on the mean velocities.

The turbulent kinetic energy and dissipation profiles in Figure 25 and the conditional-mean turbulent frequency profiles in Figure 26 are good tests of the turbulent frequency model. Both the revised and original conditional-mean turbulent frequency models are found to give good results with a proper specification of the model parameters. The variable form for  $C_{\Omega}$  has the effect of forcing  $\langle \omega \rangle$  to equal  $\Omega$  across the central region of the flow, while hardly altering the conditional-mean. Therefore, the model has little effect on the evolution of the flow. The change in  $C_{\omega 2}/C_{\omega 1}$ , however has a large impact on the peak of the conditional-mean turbulent frequency, which effects the kinetic energy and dissipation profiles.

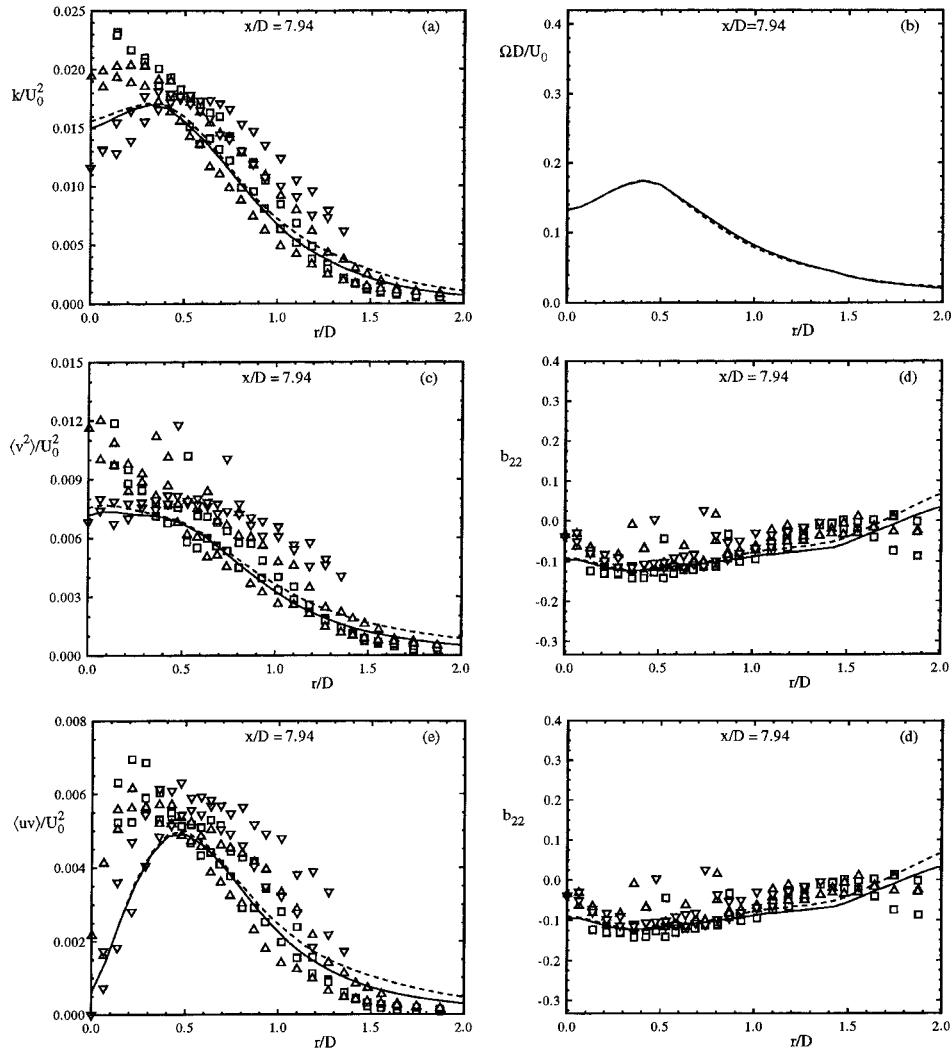


Figure 23. Predicted profiles with and without pressure transport modeling in the swirling co-axial jet: (a)  $k$ ; (b)  $\Omega$ ; (c)  $\langle v^2 \rangle$ ; (d)  $b_{22}$ ; (e)  $\langle uv \rangle$ ; and (f)  $b_{12}$ ; at  $x/D = 7.94$  for cases: —, W30a (with pressure transport), and - - -, W30d (without pressure transport); compared to experimental data of Takahashi et al. [31] with conditioning on:  $\square$ , co-flow;  $\triangle$ , annular flow; and  $\nabla$ , jet flow.

#### 4. Conclusions

The velocity/turbulent-frequency and the velocity/wave-vector/turbulent-frequency PDF methods are successfully applied to swirling and nonswirling co-axial jets and the temporal shear layer. The particular velocity models implemented include the simplified Langevin model (SLM), the Lagrangian isotropization of production model (LIPM), and the Langevin velocity wave vector

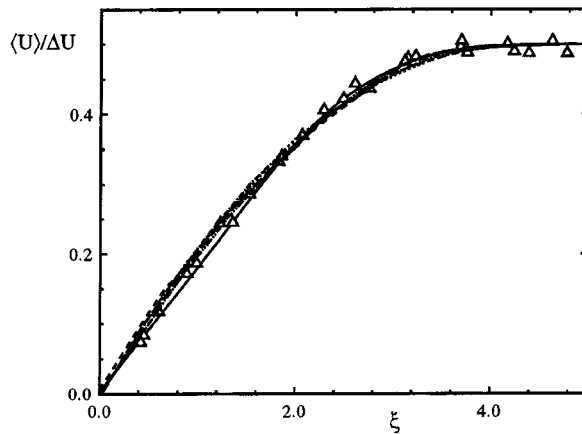


Figure 24. Self-similar mean velocity profile in the temporal shear layer for cases: —, TSc; ---, TSb; - - -, TSc; · · ·, TSd; and - · - ·, TSe; with: —, DNS data of Rogers and Moser [23]; and  $\Delta$ , experimental data of Bell and Mehta [32].

model (WVM). Revisions to the conditional-mean turbulent frequency model of Jayesh and Pope [27] are also implemented for the purpose of improving on both the numerical and the modeling performance in inhomogeneous flows. In the revised model, the production-to-dissipation ratio replaces the square of the strain rate in the modeled source of turbulent frequency to reduce the grid dependency of the bias [29], and the coefficient in the definition of the conditional-mean is defined as a function of the normalized variance of the particle turbulent frequency. A purpose of this paper is to test the implementation of the revised turbulence frequency model and not to provide a detailed numerical analysis on the bias. The pressure transport model in [2] is also tested in the co-axial jets.

The original and revised turbulent frequency models are demonstrated to perform comparably provided that the model parameters are appropriately specified. The specification of the ratio  $C_{\omega 2}/C_{\omega 1}$  is shown to be crucial in accurately modeling the co-axial jets and to be important in predicting the kinetic energy and dissipation for the temporal shear layer. This ratio represents the relative importance of destruction and production of the turbulent frequency in the modeled source of turbulent frequency, and controls the modeled production-to-dissipation of turbulent kinetic energy ratio. The suggested values for the model parameters that yield good results in both the temporal shear layer and the co-axial jets are provided in Table I. For a particular flow, an optimal specification of the parameter ratio could be determined for each of the velocity and turbulent frequency models. The results are anticipated to improve on those presented here, but the value of this ratio would be case dependent. A fundamental idea of turbulence modeling is the creation of robust models, and case dependent parameter specifications are undesirable. The optimal parameter ratio also does not imply an optimal model for the dissipation, but rather a model that minimizes the combined errors of all

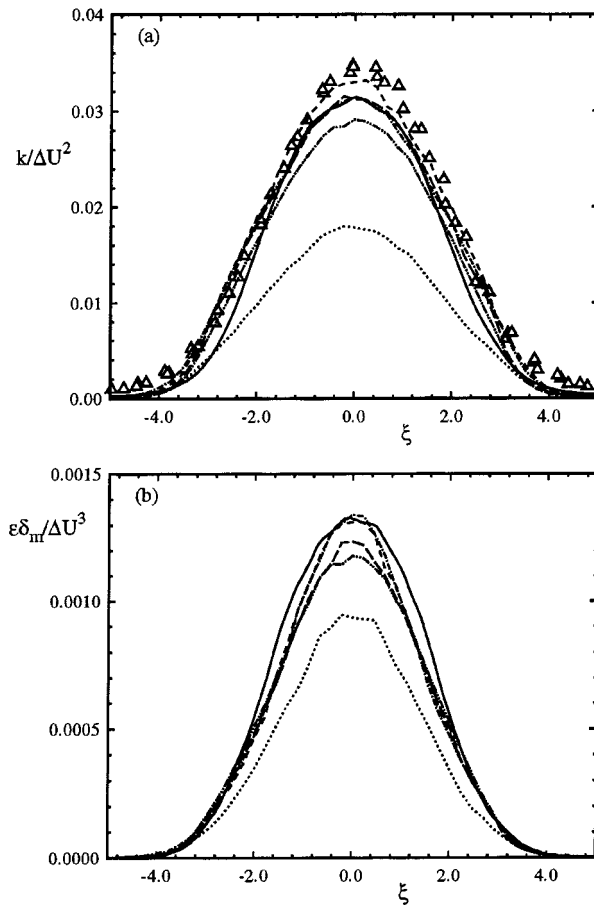


Figure 25. Self-similar profiles of: (a) turbulent kinetic energy; and (b) dissipation; in the temporal shear layer for cases: ---, TSA; -·-, TSb; ---, TSc; ···, TSd; and -·-·-, TSe; with —, DNS data of Rogers and Moser [23]; and  $\Delta$ , experimental data of Bell and Mehta [32].

other models. To correctly test the performance of turbulence modeling at the Reynolds stress level, the modeled Reynolds stress budget should be compared to experimental and/or DNS data. The profiles of the dissipation alone would be of tremendous use to modeling efforts.

The specification of  $C_\Omega$  as a function of the normalized variance is shown to have little impact on the evolution of the co-axial jets and the temporal shear layer. In the temporal shear layer, the model mean turbulent frequency is altered, while the conditional-mean is little changed. Therefore, the model has little impact on the evolution of the flow. The model is presented here to illustrate that the definition of the conditional-mean is rather robust.

The WVM is demonstrated in [2] to predict the experimental and DNS data for the temporal shear layer slightly better than the LIPM and much better than the

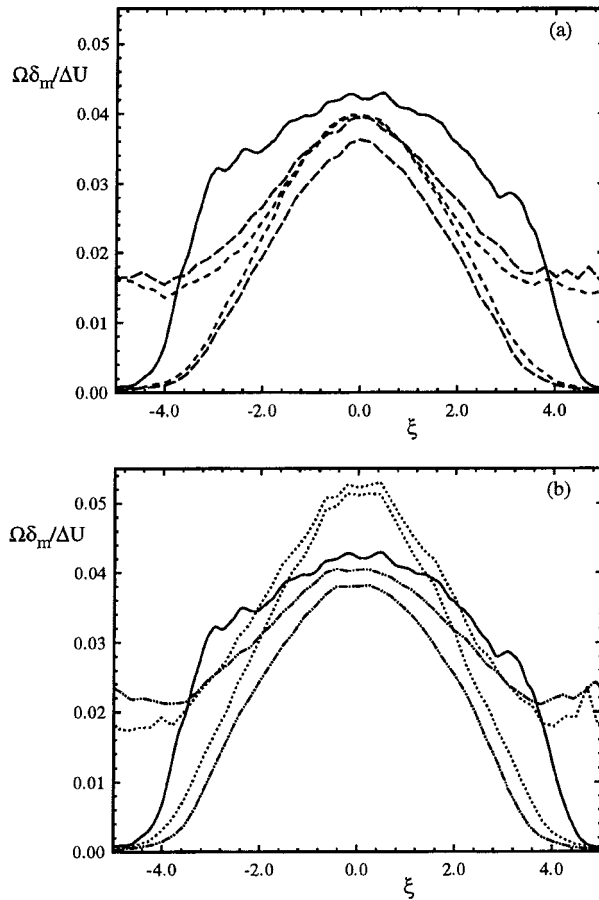


Figure 26. Self-similar profiles of the conditional-mean turbulent frequency for cases: (a) ---, TSa and - · -, TSc, and (b) · · ·, TSd and - · · -, TSe; with —, DNS data of Rogers and Moser [23].

SLM. In the case of the co-axial jets presented here, the effects of the different velocity models are secondary to the proper specification of the model parameters in turbulent frequency model. The SLM, LIPM, and WVM data shown here and SLM data from Anand et al. [10] illustrate that the mean axial velocity profiles are predicted quite well for all velocity models, while the peak mean tangential velocity decays too quickly in the SLM. A better test of the velocity models is a comparison of the Reynolds stress anisotropies. For the nonswirling jet, the WVM predicts the anisotropies better than the LIPM and SLM, but for the swirling jet all of the models are comparable. The pressure transport model is also demonstrated to be of secondary importance in these cases.

Previous studies demonstrated that standard RSMs have difficulty in predicting strongly swirling flows due to the modeling of the rapid pressure-rate-of-strain

correlation. The WVM provides an exact representation of this correlation for rapidly distorted homogeneous turbulence. However, the swirling jet cases studied here have relatively weak swirl with no vortex breakdown, and there is no clear distinction between the LIPM and the WVM. It is anticipated that the predictive capability of the SLM and LIPM will degrade in more strongly swirling flows, and additional comparisons are required to test the behavior of the WVM.

### Acknowledgments

This work was supported in part by the Department of Defense through the Air Force Graduate Fellowship Program, by NASA through its Space Grant Program, and by the Air Force Office of Scientific Research, Grant F49620-97-1-0126.

### References

1. Van Slooten, P.R. and Pope, S.B., PDF modeling for inhomogeneous turbulence with exact representation of rapid distortions. *Phys. Fluids* **9**(4) (1997) 1085.
2. Van Slooten, P.R., Jayesh and Pope, S.B., Advances in PDF modeling for inhomogeneous turbulent flows. *Phys. Fluids* **10**(1) (1998) 246.
3. Pope, S.B., PDF methods for turbulent reactive flows. *Prog. Energy Combust. Sci.* **11** (1985) 119.
4. Pope, S.B., Lagrangian PDF methods for turbulent flows. *Ann. Rev. Fluid Mech.* **26** (1994) 23.
5. Pope, S.B., A Lagrangian two-time probability density function equation for inhomogeneous turbulent flows. *Phys. Fluids* **26** (1983) 3448.
6. Haworth, D.C. and Pope, S.B., A generalized Langevin model for turbulent flows. *Phys. Fluids* **29**(2) (1986) 387.
7. Pope, S.B., On the relationship between stochastic Lagrangian models of turbulence and second-moment closures. *Phys. Fluids* **6**(2) (1994) 973.
8. Wouters, H.A., Peeters, T.W.J. and Roekaerts, D., On the existence of a stochastic Lagrangian model representation for second-moment closures. *Phys. Fluids* **8**(7) (1996) 1702.
9. Haworth, D.C. and Pope, S.B., A pdf modeling study of self-similar turbulent free shear flows. *Phys. Fluids* **30**(4) (1987) 1026.
10. Anand, M.S., Pope, S.B. and Mongia, H.C., PDF calculations for swirling flows. AIAA Paper No. 93-0106 (1993).
11. Anand, M.S., Takahashi, F., Vangsness, M.D., Durbin, M.D. and Schmoll, W.J., An experimental and computational study of swirling hydrogen jet diffusion flames. *J. Engrg. Gas Turbine and Power* (1997) 119. Also, ASME Paper No. 95-GT-307 (1995)
12. Anand, M.S., Hsu, A.T. and Pope, S.B., Calculations of swirl combustors using joint velocity-scalar probability density function method. *AIAA J.* **35**(6) (1997) 1143.
13. Fu, S. and Pope, S.B., Computation of recirculating swirling flow with the GLM Reynolds stress closure. *Acta Mech. Sinica* **10** (1994) 110.
14. Norris, A.T. and Pope, S.B., Modeling of extinction in turbulent flames by the velocity-dissipation-composition PDF method. *Combust. Flame* **100** (1995) 211.
15. Minier, J.P. and Pozorski, J., Analysis of a PDF model in a mixing layer case. In: *Tenth Symposium on Turbulent Shear Flows* (1995) p. 26.
16. Masri, A.R., Subramaniam, S. and Pope, S.B., A mixing model to improve PDF simulation of turbulent diffusion flames. In: *Twenty-Sixth Symposium (International) on Combustion* (1996) p. 49.

17. Delarue, B. and Pope, S.B., Calculations of subsonic and supersonic turbulent reacting mixing layers using probability density function methods. *Phys. Fluids* **10**(2) (1998) 487.
18. Dreeben, T.D. and Pope, S.B., PDF/Monte Carlo simulation of near-wall turbulent flows. *J. Fluid Mech.* **357** (1998) 141.
19. Launder, B.E. and Morse, A.P., Numerical prediction of axisymmetric free shear flows with a Reynolds stress closure. In: *Turbulent Shear Flows 1*. Springer-Verlag, Berlin (1979) p. 279.
20. Jones, W.P. and Pascau, A., Calculation of confined swirling flows with a second moment closure. *J. Fluids Engrg.* **111** (1989) 248.
21. Ohtsuka, M., Numerical analysis of swirling non-reacting and reacting flows by the Reynolds stress differential method. *Internat. J. Heat Fluid Flow* **38**(2) (1995) 331.
22. Kassinos, S.C. and Reynolds, W.C., A structure-based model for the rapid distortion of homogeneous turbulence. Technical Report TF-61, Stanford University (1994).
23. Rogers, M.M. and Moser, R.D., Direct simulation of a self-similar turbulent mixing layer. *Phys. Fluids* **6**(2) (1994) 903.
24. Lumley, J.L., Computational modeling of turbulent flows. In: *Advances in Applied Mechanics*, Vol. 18, Academic Press (1978) p. 123.
25. Pope, S.B. and Chen, Y.L., The velocity-dissipation probability density function model for turbulent flows. *Phys. Fluids A* **2**(8) (1990) 1437.
26. Pope, S.B., Application of the velocity-dissipation probability density function model to inhomogeneous turbulent flows. *Phys. Fluids A* **3**(8) (1991) 1947.
27. Jayesh and Pope, S.B., Stochastic model for turbulent frequency. Technical Report FDA 95-05, Cornell University (1995)
28. Delarue, B. and Pope, S.B., Application of PDF methods to compressible turbulent flows. *Phys. Fluids* **9**(9) (1997) 2704.
29. Xu, J. and Pope, S.B., Sources of bias in particle-mesh methods for PDF models for turbulent flows. Technical Report FDA 97-01, Cornell University (1997).
30. Takahashi, F. and Vangness, M.D., Measurements in swirling and non-swirling coaxial turbulent air jets – No. 1: No swirl, 100 m/s. Technical Report UDR-TR-91-160, University of Dayton, Ohio (1991).
31. Takahashi, F., Vangness, M.D. and Belovich, V.M., Measurements in swirling and non-swirling coaxial turbulent air jets – No. 3: 30-degree swirl, 100 m/s. Technical Report UDR-TR-91-162, University of Dayton, Ohio (1991).
32. Bell, J.H. and Mehta, R.D., Development of a two-stream mixing layer from tripped and untripped boundary layers. *AIAA J.* **28**(12) (1990) 2034.
33. Pope, S.B., PDF2DV: A FORTRAN code for solving modeled joint-PDF equations in two-dimensions. Cornell University (1994).
34. Dreeben, T.D. and Pope, S.B., Nonparametric estimation of mean fields with application to particle methods for turbulent flows. Technical Report FDA 92-13, Cornell University (1992).
35. Pope, S.B., Position, velocity and pressure correction algorithm for particle method solution of the PDF transport equations. Technical Report FDA 95-06, Cornell University (1995).
36. Naot, D., Shavit, A. and Wolfshtein, M., Interactions between components of the turbulent velocity correlation tensor. *Israel J. Tech.* **8** (1970) 259.
37. Launder, B.E., Reece, G.J. and Rodi, W., Progress in the development of a Reynolds-stress turbulence closure. *J. Fluid Mech.* **68**(3) (1975) 537.
38. Shih, T.H. and Lumley, J.L., Modeling of pressure correlation terms in Reynolds stress and scalar flux equations. Technical Report FDA 85-3, Cornell University (1985).
39. Fu, S., Launder, B.E. and Tselepidakis, D.P., Accommodating the effects of high strain rates in modelling the pressure-strain correlation. Technical Report TFD/87/5 and TDF/89/1, UMIST (1987).
40. Speziale, C.G., Sarkar, S. and Gatski, T.B., Modelling the pressure-strain correlation of turbulence: An invariant dynamical systems approach. *J. Fluid Mech.* **227** (1991) 245.

41. Johansson, A.V. and Hällback, M., Modelling of rapid pressure-strain in Reynolds-stress closures. *J. Fluid Mech.* **269** (1994) 143.
42. Ristorcelli, J.R., Lumley, J.L. and Abid, R., A rapid-pressure covariance representation consistent with the Taylor–Proudman theorem materially indifferent in the two-dimensional limit. *J. Fluid Mech.* **292** (1995) 111.
43. Yeung, P.K. and Pope, S.B., Lagrangian statistics from direct numerical simulations of isotropic turbulence. *J. Fluid Mech.* **207** (1989) 531.
44. Hanjalić, K. and Launder, B.E., A Reynolds stress model of turbulence and its applications. *J. Fluid Mech.* **52** (1972) 609.
45. Dimotakis, P.E., Turbulent free shear layer mixing and combustion. In: Murthy, S.N.B. and Curran, E.T. (eds), *High-Speed-Flight Propulsion Systems*, AIAA, Washington, DC (1991) p. 265.